Atmos. Chem. Phys. Discuss., 15, 27449–27499, 2015
www.atmos-chem-phys-discuss.net/15/27449/2015/
doi:10.5194/acpd-15-27449-2015

Atmospheric Chemistry and Physics Discussions

Aerosol–radiation–cloud interactions in a regional coupled model: the effects of convective parameterisation and resolution

S. Archer-Nicholls[1,a], **D. Lowe**[1], **D. M. Schultz**[1], **and G. McFiggans**[1]

[1]Centre for Atmospheric Sciences, School of Earth, Atmospheric and Environmental Sciences, University of Manchester, Manchester, UK
[a]now at: National Centre for Atmospheric Research (NCAR), Boulder, CO, USA

Received: 3 September 2015 – Accepted: 13 September 2015 – Published: 13 October 2015

Correspondence to: G. McFiggans (g.mcfiggans@manchester.ac.uk)

Published by Copernicus Publications on behalf of the European Geosciences Union.

Abstract

The Weather Research and Forecasting model with Chemistry (WRF-Chem) has been used to simulate a region of Brazil heavily influenced by biomass burning. Nested simulations were run at 5 km and 1 km horizontal grid spacing for three case studies in September 2012. Simulations were run with and without fire emissions, convective parameterisation on the 5 km domain and aerosol–radiation interactions in order to explore the differences attributable to the parameterisations and to better understand the aerosol direct effects and cloud responses. Direct aerosol–radiation interactions due to biomass burning aerosol resulted in a net cooling, with an average reduction of downwelling shortwave radiation at the surface of $-24.7\,W\,m^{-2}$ over the three case studies. However, around $21.7\,W\,m^{-2}$ is absorbed by aerosol in the atmospheric column, warming the atmosphere at the aerosol layer height, stabilising the column, inhibiting convection and reducing cloud cover and precipitation. The changes to clouds due to radiatively interacting aerosol (traditionally known as the semi-direct effects) increase net shortwave radiation reaching the surface by reducing cloud cover, producing a secondary warming that largely counters the direct cooling. However, the magnitude of the semi-direct effect was difficult to quantify, being extremely sensitive to the model resolution and use of convective parameterisation. The 1 km domain simulated clouds less horizontally spread, reducing the proportion of the domain covered by cloud in all scenarios and producing a smaller semi-direct effect. Not having a convective parameterisation on the 5 km domain reduced total cloud cover, but also total precipitation. BB aerosol particles acted as CCN, increasing the droplet number concentration of clouds. However, the changes to cloud properties had negligible impact on net radiative balance on either domain, with or without convective parameterisation. Sensitivity to the uncertainties relating to the semi-direct effect was greater than any other observable cloud adjustments. Although WRF-Chem currently lacks aerosol–cloud interactions in parameterised clouds, the results of this study suggest a greater priority for development is to improve the modelling of semi-direct effects by reducing the uncertainties

ACPD
15, 27449–27499, 2015

relating to use of convective parameterisation and resolution before WRF-Chem can reliably quantify the regional impacts of aerosols.

1 Introduction

Aerosol particles in the atmosphere have a major impact on global climate, but also contribute some of the greatest uncertainties due to their heterogeneous distribution and complicated interactions with clouds and radiation (IPCC, 2013). The aerosol–radiation interactions, commonly known as the direct effects, tend to result in scattering of solar radiation and cooling of the Earth's surface (Haywood and Boucher, 2000; Zhang et al., 2008; Chand et al., 2009). However, many aerosol particles also contain black carbon (BC), which absorbs radiation across a wide spectrum of wavelengths (Bond et al., 2013). Whether an absorbing aerosol layer has a net cooling or warming effect, as seen from the top-of-atmosphere (TOA), depends greatly on whether it is over a low or high albedo surface (Haywood et al., 1995; Haywood and Boucher, 2000).

As well as their direct interactions with radiation, aerosol particles can perturb the Earth's radiative budget through their impacts on clouds (Lohmann and Feichter, 2005; Rosenfeld et al., 2008; IPCC, 2013; Possner et al., 2015). The absorption and scattering of radiation changes atmospheric stability and circulation, and therefore cloud formation. These adjustments by the climate system are traditionally known as the semi–direct effects (Hansen et al., 1997; Ackermann et al., 2000). The sign and magnitude of the semi-direct radiative forcings are sensitive to whether the aerosol layer is over land or sea (Allen and Sherwood, 2010), and to the vertical distribution, depending on whether the aerosol layer is below, at or above cloud height (Johnson et al., 2004; Koch and Del Genio, 2010). In addition, aerosol particles act as cloud condensation nuclei (CCN, Andreae et al., 2004; McFiggans et al., 2006; Hennigan et al., 2012). Polluted clouds have increased cloud droplet number, resulting in the first indirect effect whereby brighter clouds reflect more radiation back to space (Twomey, 1974; Lohmann and Feichter, 2005; Possner et al., 2015). Increased droplet number

ACPD
15, 27449–27499, 2015

may further perturb cloud lifetime, height and the ability to initiate precipitation (Andreae and Rosenfeld, 2008; Chen et al., 2011). The addition of aerosol particles can either inhibit or enhance cloud formation: a small increase in CCN above pristine conditions in deep convective clouds cause more droplets to reach supercooled levels, increasing the amount of latent heat release and invigorating convection (Rosenfeld et al., 2008; Pöschl et al., 2010; Possner et al., 2015). Rosenfeld et al. (2008) estimate the maximum invigoration point to be at a CCN concentration of 0.4 % supersaturation ($CCN_{0.4}$) of approximately 1200 cm^{-3}. Further increases in CCN result in the direct radiative effects dominating, which cool the surface and inhibit convection.

The primary tool for estimating aerosol particles' impact on climate has been the use of global climate models (IPCC, 2013, and references therein). However, horizontal grid spacing is typically in the order of a degree, meaning most clouds are smaller than a grid box and must be parameterised, introducing uncertainties to how the system responds to forcings by aerosol particles (Johnson, 2004; Ghan et al., 2006; Lohmann and Ferrachat, 2010). For example, the magnitude and sign of the semi-direct effects show strong sensitivity to the cloud parameterisation used (Cook et al., 2004).

At the other end of the resolution spectrum, large eddy simulation (LES) models are capable of explicitly resolving clouds with detailed bin microphysics at grid spacings in the order of 10–100 m. Although LES models can only be used over small areas, often with idealised boundary conditions, they are useful to gain insight into how aerosols affect clouds and are known to reproduce more realistic behaviour than the parameterisations used in global models (Romakkaniemi et al., 2009; Chen et al., 2011). Johnson (2004) compared a single-column model, equivalent to a cloud parameterisation used in global models, with a LES model, and found the semi-direct effect over a stratocumulus deck was five times stronger in the LES simulation, implying deficiencies in the ability of global models to parameterise aerosol–cloud interactions.

The need to better understand the impact of aerosol–radiation–cloud interactions on a regional scale has driven the development of "online" models with "full" couplings between the air quality and meteorological components (Baklanov et al., 2011, 2013;

ACPD
15, 27449–27499, 2015

Grell and Baklanov, 2011). The Weather Research and Forecasting model with Chemistry (WRF-Chem) is one such model (Grell et al., 2005; Fast et al., 2006). Unlike in offline chemical transport models, the gas-phase chemical and aerosol fields are transported using the same timestep and physical parameterisations as the core numerical weather prediction model. By linking aerosol optical properties to the radiation scheme and CCN potential to the microphysics scheme, feedbacks between aerosols and meteorology can be modelled (Chapman et al., 2009; Barnard et al., 2010; Zhao et al., 2011). However, WRF-Chem is currently limited by having no aerosol–cloud interactions in parameterised convective clouds, and no linkages exist in the model between aerosol particles and ice nuclei (Chapman et al., 2009). Studies into indirect effects with WRF-Chem have therefore tended to focus on marine stratocumulus, which can be resolved at coarser resolutions (e.g. Yang et al., 2011; Saide et al., 2012).

As computing resources have improved, WRF-Chem has been increasingly run at fine resolutions with horizontal grid spacings less than 10 km (e.g. Grell et al., 2011; Wu et al., 2011a, b; Saide et al., 2012; Shrivastava et al., 2013; Fast et al., 2014). These scales (commonly known as the "grey-zone") are challenging to model because the assumptions behind the deep-convective parameterisations begin to break down, but the model cannot be expected to resolve all convection explicitly (Hong and Dudhia, 2012). The Grell-3-D convective parameterisation has in part been developed to be used over these intermediate horizontal resolutions by allowing "subsistence spreading" to neighbouring grid cells (Grell and Freitas, 2014). However, it is currently unclear how effectively cloud responses to aerosol in the "grey-zone" are simulated with this parameterisation. Through further nesting, WRF-Chem can be run at scales where no cumulus parameterisation should be used ($\Delta x \lesssim 4$ km), bridging the gap between global climate and LES models to explicitly resolve aerosol–cloud interactions in warm convective clouds. However, even at these fine scales questions remain as to how well some structures, such as shallow cumulus clouds, are simulated (Hong and Dudhia, 2012).

ACPD
15, 27449–27499, 2015

This purpose of this study is to critically evaluate how regional aerosol–radiation–cloud interactions are captured in WRF-Chem, using a period during the South American Biomass Burning Analysis (SAMBBA) project as an example. The modelled aerosol direct, semi-direct and indirect effects are calculated as a function of horizontal grid spacing and cumulus parameterisations – both with and without fire emissions – illustrating the uncertainties in representing these processes within models and making accurate predictions. As a result, this study educates WRF-Chem users as to the strengths and weaknesses of the processes within the model, providing an impetus for further developments to improve simulations in these challenging regimes.

The test case used is a region of Brazil known to be heavily polluted by biomass burning aerosol (BBA) during the dry season. The aerosol haze layer is characterised as being highly radiatively absorbing (single scattering albedo between 0.8 and 0.9), optically thick (aerosol optical depths between 0.4 and 1.2), vertically elevated to cloud-level through biomass burning plume processes, and efficient at acting as CCN (Reid et al., 2005a, b; Martin et al., 2010; Archer-Nicholls et al., 2015). The high aerosol concentrations in this region should provide a strong signal for aerosol–radiation and aerosol–cloud interactions for the study.

WRF-Chem has been previously used to investigate the impact of BBA on weather and climate. For example, Grell et al. (2011) found a significant improvement to the modelled representation of the vertical temperature profile when biomass burning emissions and aerosol feedbacks were included in runs over Alaska. Zhang et al. (2014) evaluated the direct radiative effects of BBA over Northern Sub-Saharan Africa, and impacts to vary widely depending on the emission inventory used. Wu et al. (2011b) ran simulations over Brazil at 36 and 4 km horizontal grid spacing, with no convective parameterisation on the 4 km domain. They found BBA to inhibit afternoon convection over the domain, reducing daytime precipitation but increasing it night, albeit with a net decrease in precipitation. The 36 and 4 km simulations were qualitatively similar.

ACPD
15, 27449–27499, 2015

This paper follows on from Archer-Nicholls et al. (2015), which aimed to characterise the BBA population in Brazil in the 2012 fire season. The model output was evaluated against remote sensing and in-situ aircraft measurements from the SAMBBA campaign. The initial setup, using the Brazilian Biomass Burning Emissions Model (3BEM) with Freitas et al. (2007) plume-rise parameterisation resulted in injection of fire emissions too high into the atmosphere compared to aircraft measurements. An alternative emissions scenario, using reduced fire size based on remote-sensing measurements of fire radiative products for the 2012 dry season, was developed and compared with measurements, showing an improved vertical distribution but still with some bias towards having too much aerosol between 2–6 km. The particulate organic matter to BC ratio was lower in model compared to measurement, likely due to uncertainties in biomass burning emission factors and lack of secondary organic aerosol (SOA) formation in the model. However, the single scattering albedo ω_0 was similar to that measured. Aerosol size distribution and CCN concentration were both reasonably well represented.

The model fields from Archer-Nicholls et al. (2015) are used to drive initial and boundary conditions for two nested domains with 5 km and 1 km horizontal grid spacing in this study. The 5 km domain was chosen to be within the "grey-zone" in order to probe how the WRF-Chem simulates aerosol interactions and impacts, while the 1 km domain has no need for a convective parameterisation. Several runs were conducted using different emission scenarios and options for aerosol–radiation interactions to separate the instantaneous radiative effects of the aerosol from aerosol–cloud interactions. The sensitivity of the semi-direct and indirect effects to convective parameterisation and horizontal resolution is also investigated. Due to the limited area and duration of the model runs, simulating the full changes to circulation as a result of the forcings are out of the scope of the current study and so only short-term responses are investigated.

ACPD
15, 27449–27499, 2015

2 Model description

This study uses WRF-Chem version 3.4.1 with changes made to use the Model for Simulating Aerosol Interactions with Chemistry (MOSAIC) aerosol scheme (Zaveri et al., 2008) and the updated Carbon Bond Mechanism (CBM-Z) gas phase chemistry scheme (Zaveri and Peters, 1999) with the Brazilian Biomass Burning Model (3BEM) fire emissions (Longo et al., 2010; Freitas et al., 2011), as described by Archer-Nicholls et al. (2015). As an "online" coupled model, the meteorological, transport, chemical and aerosol components are integrated at the same time. Forcings from the chemical and aerosol fields can feed-back with the meteorology, and visa-versa (Grell et al., 2005). These feedbacks primarily occur through the aerosol–radiation interactions and aerosol particles acting as CCN to influence cloud properties. A robust approach to describe the aerosol population and their interactions with clouds and radiation is therefore needed.

2.1 The MOSAIC aerosol mechanism

The MOSAIC mechanism is a sectional scheme, whereby the aerosol size distribution is described as a set of discrete size bins (Zaveri et al., 2008). This study uses eight size bins across a range of 39 nm to 10 µm, as shown in Table 1. MOSAIC carries five inorganic ions which can react in the aqueous phase and partition with the gas-phase mechanism, plus three unreactive primary aerosol species: black carbon (BC), particulate organic matter (POM), and other inorganics (OIN) (Fast et al., 2006; Zaveri et al., 2008). All chemical components within each size bin are assumed to be internally mixed (i.e. evenly mixed within the same particles), whilst different size bins are assumed to be externally mixed (Zaveri et al., 2008). The version of MOSAIC used in this study does not carry secondary organic aerosol (SOA). Current conventional treatments are unable to capture frequently observed SOA behaviour, such as the formation of sufficient mass from known precursors or the oxygen to carbon ratio (O : C) of the material. Alternative treatments are available, such as the Volatility Basis Set

ACPD
15, 27449–27499, 2015

(VBS Donahue et al., 2011; Shrivastava et al., 2011, 2013), but remain unconstrained for the current application. In particular, it is unclear how previously used treatments can capture behaviour such as that summarised in the meta-analysis of Jolleys et al. (2012), which described the lack of increase in organic mass from biomass burning source, but an increase in O : C. Ongoing developments of the VBS are in progress to explore mechanisms by which observed OA behaviour is best captured, but are beyond the scope of the current work. However, it is expected that the current approach will reasonably capture the OA mass and hence POM : BC ratio.

Whilst uncertainties in the model representation of aerosol composition (particularly POM : BC ratio), size distribution and optical properties can result in uncertainties in predicted radiative forcings (Matsui et al., 2013; Kodros et al., 2015), investigation of these uncertainties is beyond the scope of the current study. Notwithstanding the discussed limitations, using a sectional representation of aerosol provides a reasonably robust approach for calculating the aerosol optical properties and interactions with clouds, as described below.

2.2 Calculation of aerosol optical properties

Within MOSAIC, each aerosol chemical component has its own associated complex refractive index, with BC being the most absorbing (Barnard et al., 2010). The overall complex refractive index is calculated for each bin using a mixing rule to approximate the internal structure of the aerosol particles. Assuming an internal mixture of BC with other components can result in an overestimation of the particles absorption cross-section (Bond and Bergstrom, 2006). Describing particles using a spherical BC core with other component shell (a "shell-core" mixing rule) is often regarded as the most robust approach for 3-D model applications (Bond et al., 2006; Bond and Bergstrom, 2006; Barnard et al., 2010; Matsui et al., 2013), but was found to be unstable in WRF-Chem version 3.4.1. In this study, the Maxwell–Garnett mixing rule is used, whereby aerosol particles are assumed to be made up of randomly distributed spheres of BC throughout a mixture of all other components (Bohren and Huffman, 1983, chapter 8).

ACPD
15, 27449–27499, 2015

The Maxwell–Garnett rule does not suffer from the anomalous absorption enhancement of the internal mixing rule (Bond and Bergstrom, 2006).

Mie calculations are used to calculate the intermediate optical properties for each bin, which are summed over all size bins to give bulk extinction coefficient (b_{ext}), scattering coefficient (b_s), single scattering albedo ($\omega_0 = b_s/b_{ext}$), and asymmetry factor (g). Each of these variables are functions of the size parameter ($x = 2\pi r/\lambda$), where λ is the wavelength of light and r is the wet radius at the centre of the aerosol bin (Fast et al., 2006). To save on computation, the methodology of Ghan et al. (2001) is employed to carry out the full Mie calculations only on the first call to the subroutine. The net radiative impacts are calculated by passing the bulk optical properties of the aerosol layer to the radiative transfer parameterisation. This study uses the rapid radiative transfer model (RRTMG, Mlawer et al., 1997; Iacono et al., 2000) for both short-wave (SW) and long-wave (LW) radiation following Zhao et al. (2011). Optical properties in the SW are calculated at four wavelengths (λ = 300, 400, 600, and 1000 nm). For intermediate λ, b_{ext} is estimated using an Ångström coefficient, whereas ω_0 and g are linearly interpolated. A full description of the optical property calculations are given by Fast et al. (2006) and Barnard et al. (2010).

2.3 Calculation of aerosol–cloud interactions

A key process to simulating aerosol–cloud interactions is the activation of CCN to form cloud droplets. Köhler et al. (1936) theory describes the equilibrium state of an aerosol particle, assumed to be an aqueous salt solution, with ambient water vapour. The critical supersaturation (S_{crit}, defined as the supersaturation at which an aerosol particle becomes activated to form a cloud droplet) depends upon both aerosol size and composition. Aerosol particles that are larger and/or more hygroscopic are activated more easily and so have a lower S_{crit} (McFiggans et al., 2006). Within MOSAIC, S_{crit} is calculated for each bin using a mass-weighted average of the associated hygroscopicity of all chemical components within that bin using the methodology of (Abdul-Razzak and Ghan, 2002).

ACPD
15, 27449–27499, 2015

The primary driver of cloud droplet activation is the updraft velocity (w): air parcels with higher w reach higher maximum supersaturations (S_{max}). All particles with $S_{crit} < S_{max}$ will be activated, whereas those with $S_{crit} > S_{max}$ remain unactivated within clouds and are known as interstitial aerosols (Chapman et al., 2009). Greater CCN concentration increases the total particulate surface area, increasing competition for condensable water and reducing S_{max}. Subgrid variation in updraft velocity (w) is described using a Gaussian distribution function, with a minimum spread of $\sigma_w = 0.1\,\mathrm{m\,s^{-1}}$ (Ghan et al., 1997). The number and mass fraction of activated CCN in each aerosol bin can then be calculated by comparing S_{max} with S_{crit} at the sectional limits of each bin (Abdul-Razzak and Ghan, 2002). Inversely, this method can also estimate the CCN concentration at given supersaturations. WRF-Chem caries six diagnostic variables showing the concentration of particles that can potentially activate at given supersaturations of 0.02, 0.05, 0.1, 0.2, 0.5 and 1 % ($CCN_{0.02}$, $CCN_{0.05}$, $CCN_{0.1}$, $CCN_{0.2}$, $CCN_{0.5}$ and $CCN_{1.0}$ respectively).

Recently, Simpson et al. (2014) have shown the Abdul-Razzak and Ghan (2000) parameterisation produces unrealistic activated fractions of aerosol in some atmospherically relevant conditions when compared with an explicit bin-resolving cloud-parcel model. The scheme was shown to over predict activation when the aerosol population median diameter was $\gtrsim 300$ nm. However, given the median diameter in BBA populations is generally between 100–150 nm (Janhall et al., 2010), this behaviour should not negatively impact the simulations in this study.

To model the indirect effects the cloud activation scheme needs to be coupled with a double-moment microphysical parameterisation that carries both number and mass loadings for hydrometeors. Following Yang et al. (2011), the double-moment Morrison et al. (2005, 2009) parameterisation has been coupled with MOSAIC aerosol, such that the number concentration of liquid droplets is controlled by activated aerosol. The couplings are currently only for warm-cloud processes, with no direct links between aerosol and ice nuclei (Chapman et al., 2009). A major limitation in using WRF-Chem to assess aerosol–cloud interactions is that the couplings are only computed in explic-

ACPD
15, 27449–27499, 2015

itly resolved clouds, not convective clouds simulated by the cumulus parameterisation (Chapman et al., 2009; Yang et al., 2011). Work is being conducted to include aerosol interactions with parameterised cloud (e.g. Grell and Freitas, 2014; Berg et al., 2014). However, these developments were not available for general WRF-Chem release at the time of this study.

3 Experimental Setup

This section describes the model setup and rationale for the experiments conducted for this study. The objective is to probe the response of the WRF-Chem model to aerosol–radiation and aerosol–cloud interactions across a range of scales and meteorological conditions. The high levels of elevated, highly-absorbing aerosol over Amazonia during the dry-to-wet season transition provide a good test-bed for the experiments by producing a strong signal of aerosol forcings. Several scenarios were constructed to isolate the various aerosol impacts, as described below.

3.1 Domain setup

Archer-Nicholls et al. (2015) described a parent domain run for the whole of September 2012 with 226 × 196 grid cells at 25 km horizontal grid spacing covering most of South America, 41 vertical levels up to 50 hPa with 18 levels within the lowest 3 km, and a Lambert conformal conic projection. The meteorological input and boundary conditions were driven by the operational, deterministic (high-resolution) 1 day forecasts of the European Centre for Medium-Range Weather Forecasts (ECMWF, http://www.ecmwf.int/). Chemical and aerosol boundary conditions were derived from the MACC-II reanalysis (Monitoring Atmospheric Composition and Climate – Interim Implementation; Hollingsworth et al., 2008; Flemming et al., 2013).

This study focuses on the output of two nested domains, with 5 and 1 km grid spacing respectively. The location of the 5 km nest encompasses a region of high aerosol optical

ACPD
15, 27449–27499, 2015

depths (AODs) over Rondônia state. The 1 km domain is positioned over a region with high AODs, flat topography and heavy precipitation on 18 September 2012. A map of all three domains is shown in Fig. 1. The nests were run for three 36 h case-study periods with contrasting meteorological conditions, starting at 00:00 UTC on 14, 18 and 23 September 2012 respectively (where local time = UTC − 4 h). These dates coincide with the SAMBBA flight numbers B731, B734 and B739, against which the model output was evaluated by Archer-Nicholls et al. (2015). The ndown utility was used to generate hourly offline boundary conditions for the 5 km nests from the 25 km runs. The 5 and 1 km nests were run online without feedback between nests.

Except where otherwise stated, the 5 km domain uses the Grell-3-D convective scheme with subsidence spreading turned on so as to be applicable for use below 10 km grid spacing (Grell and Freitas, 2014). No convective parameterisation is used on the 1 km nest, allowing explicit aerosol–cloud interactions in convective clouds. The differences in model setup between domains are summarised in Table 2. All other physical parameterisations are the same between the nested and parent domains and are described in more detail in Archer-Nicholls et al. (2015).

3.2 Scenarios

Two emission scenarios are considered in this study: fire emissions (FE) and no fire emissions (nFE). FE uses the 3BEM fire emissions with the Freitas et al. (2007) plume-rise parameterisation and modifications for the 2012 biomass burning season described in Archer-Nicholls et al. (2015). The nFE scenario has no fire emissions, but has the same anthropogenic emissions, biogenic emissions and boundary conditions as the FE scenario. Both of these scenarios were run for the entirety of September on the 25 km domain without aerosol–radiation interactions (aer_rad_feedback = 0). The meteorological fields were reinitialised from ECMWF fields at the start of each nested simulation run to minimise synoptic-scale error growth and ensure that any differences within the nested domains were due to processes being investigated within the nests.

ACPD
15, 27449–27499, 2015

To separate the impacts of aerosol–radiation interactions from cloud–aerosol interactions, the model was run with aerosol–radiation interactions turned on and off. Unless otherwise stated, references to the FE and nFE scenarios refer to scenarios with aerosol–radiation interactions on. The scenario with no fire emissions or aerosol–radiation interactions is used as a control simulation (Ctrl), and behaves as a WRF simulation would (i.e. with negligible aerosol effects). Another scenario with fire emissions but no aerosol–radiation interactions (nARI) is used to isolate the impacts of cloud–aerosol interactions. Finally, each scenario was also run with the Grell-3-D convective parameterisation turned off over the 5 km domain (denoted with the suffix "_nCU") for the 18 September 2012 initialisation. The scenarios are summarised in Table 3.

3.3 Meteorological conditions

Figure 2 shows averaged precipitation and winds at 700 hPa over the three case study periods over the 5 km domain. The meteorological input conditions of each nested simulation case study are derived from the ECMWF data, whereas the chemical and aerosol input conditions are interpolated from the 25 km domain. The first 6 h of integration of each run are discarded as spin-up.

The modelled meteorological conditions differ markedly for each case study. The driest conditions are on 14 September, with only limited convective precipitation. Prevalent winds are easterly or north easterly. Extensive fire emissions and minimal precipitation over the region between 10 and 14 September result in high modelled aerosol loadings. By 18 September the transition into the wet season has begun, with widespread precipitation across the 5 km domain and the location of the 1 km nest, and prevailing northerly winds. Aerosol loadings are lower than on the 14 September, but still high. There is heavy precipitation and easterly winds over the northern half of the domain on 23 September, but north to north-westerly winds and little precipitation over the southern half (where the 1 km nest is located). By 23 September, prolonged rainfall has washed out much aerosol. However, the model shows higher aerosol loadings

ACPD
15, 27449–27499, 2015

compared to measurements on this date (see Archer-Nicholls et al., 2015, for more details).

4 Results

To assess how the WRF-Chem model simulates the regional impacts of BBA under various model setups and meteorological conditions, the analysis first evaluates the instantaneous direct radiative effects of aerosol–radiation interactions, temporarily ignoring the influence of clouds, in Sect. 4.1. Changes to the atmospheric stability, and how this in turn affects cloud formation and precipitation, are then presented (Sect. 4.2). The radiative balance is evaluated with regard to the cloud response to identify the semi-direct effects, testing the sensitivity of the cloud responses to resolution and convective parameterisation (Sects. 4.2 and 4.3). Finally in Sect. 4.4, aerosol–cloud interactions in the model are investigated. Output from the 5 km, 1 km domains and runs with no convective parameterisation over the 5 km domain are analysed, testing how much of an impact the lack of aerosol–cloud interactions in parameterised clouds has on the simulations.

4.1 Direct aerosol–radiative interactions and changes to atmospheric stability

Figure 3a–c shows the aerosol optical depth (AOD) at 550 nm over the 5 km domain for the FE scenario. AOD is highest on 14 September 2012, between 0.8 and 1.2 over most of the domain. The other two days are lower, between 0.4 and 1.0. Figure 3d–f show the vertical cross-section of extinction, averaged over the 5 km domain. The majority of the aerosol layer is in the lower 4 km of the atmosphere. Fresh emissions are injected at altitude during the local afternoon of each day. Note that the AOD is non-zero in the nFE scenario, generally between 0.2 and 0.4, owing to contributions from anthropogenic emissions, dust and other long-range transported aerosol.

ACPD
15, 27449–27499, 2015

Figure 4 shows maps of the differences in clear-sky (ignoring cloud effects) radiation fluxes between the FE and nFE scenarios and time-series for the four main scenarios averaged over the 5 km domain for 14 September 2012. Similar figures for 18 and 23 September are included in the Supplement. The calculations of the radiative fluxes are described in Appendix A. Downwelling clear-sky SW radiation at the surface ($SW^{\downarrow}_{Sfc,\,clr}$) on 14 September 2012 is reduced by a maximum of $-109.5\,W\,m^{-2}$ compared to the nFE scenario (Fig. 4a and d). The clear-sky radiative effects on the 18 and 23 September case studies are qualitatively similar to 14 September. The difference in clear-sky radiative balance between the FE and nFE scenarios (ΔRB_{clr}) is negative (i.e. the aerosol layer has a net cooling effect at the TOA if cloud effects are ignored; Fig. 4b and e). Although BBA is highly absorbing, it has a net negative forcing because it is predominantly over forest which has a low albedo of 0.12. Averaged over 24 h, from dawn to dawn, the difference in RB_{clr} between the FE and nFE scenarios is $-5.0\,W\,m^{-2}$, equal to the net direct forcing the aerosol layer would have if there were no clouds in the domain.

Averaged over 24 h, around $28\,W\,m^{-2}$ more SW radiation is absorbed by the atmospheric column in the FE scenario than the nFE scenario on 14 September (Fig. 4c and f), compared to 19 and $18\,W\,m^{-2}$ on 18 and 23 September respectively. The full tables of domain averaged radiative budgets are summarised in the Supplement. These results are comparable in magnitude and sign to a similar study conducted over the same case-study using the Met Office Unified Model (Kolusu et al., 2015). Overall, the net direct radiative effects of the aerosol layer are to reduce the total energy in the system, cool the surface and warm the lower troposphere.

4.2 Cloud responses to aerosol forcings

When the radiative effects of cloud fields are included, the changes to the radiative balance due to BBA are dramatically different (Fig. 5). There is little cloud cover in the mornings but large convective clouds form in the afternoon. In the mornings, ΔRB_{FE} is

ACPD
15, 27449–27499, 2015

negative and qualitatively similar to the behaviour of the clear-sky case in Fig. 4e. In the afternoon, a strong positive forcing is observed in the FE scenario as there is much reduced cloud cover resulting in less SW radiation being reflected to space (see Fig. 3 in Supplement). This difference is greatest on 18 September (the case study with the most precipitation and cloud cover across the domain), peaking at $+70\,\mathrm{W\,m^{-2}}$. This cloud response more than counters the clear-sky direct radiative cooling of the aerosol over the same period.

At nighttime, there is a net negative forcing of approximately $-10\,\mathrm{W\,m^{-2}}$ in the FE run on 18 and 23 September which occurs because there are fewer ice clouds at high altitude in the FE scenario (Fig. 5). Cirrus clouds efficiently trap LW radiation, and so the thinner ice clouds in the FE simulations result in an increase in $\mathrm{LW}^{\uparrow}_{\mathrm{TOA}}$. Whilst we are unsure of the physical significance of this effect, the forcings due to changes in nighttime ice clouds are comparable in magnitude to the daytime forcings and so have an appreciable impact on the accumulated radiative balance.

To understand the differences in radiative budget between the clear-sky and all-sky variables, we need to first understand how the aerosol layer is affecting cloud formation. Changes can be observed in the vertical profile of the domain averaged potential temperature θ (Fig. 6a–c). On each day after local sunrise (approximately 10:00 UTC) the surface layer and lower PBL is cooler in the FE scenario, and warmer between 850 and 500 hPa. The changes in θ are indicative of the aerosol layer stabilising the column, resulting in inhibition of the initiation of convection and reducing the amount of cloud (Fig. 6d–f).

On all three case studies, there was a reduction in cloud formation in the FE scenario during the onset of precipitation around 18:00 to 21:00 UTC, reducing the average cloud cover. This change is least significant on the 14 September case study, as there was less precipitation on this day compared to the others. On 18 September, the presence of BBA consistently reduces all cloud types into the night. On 23 September, there is some displacement of peak precipitation in the FE scenario, resulting in longer cloud lifetimes and some periods with greater quantities of graupel and snow in the FE

ACPD
15, 27449–27499, 2015

scenario. On 18 and 23 September, there is a reduction in nighttime high-altitude ice clouds in the FE scenario.

The 24 h averaged radiative budgets, for each scenario are summarised in Tables S1–S3 in the Supplement, with averages of basic meteorological variables in Tables S4–S6 in the Supplement. Comparing the FE scenario with the nFE and Ctrl scenarios shows the total aerosol impact. Differences between the nARI and Ctrl scenario are indicative of aerosol–cloud interactions. Comparing the 1 km domain with the same region from the 5 km domains highlights sensitivity to model resolution. On each of the case studies, more SW radiation is absorbed in the FE scenario over every domain. While $SW^{\downarrow}_{Sfc}$ is lower in the FE scenario on all days, the net changes to radiative balance (RB) are less consistent and often negligible. The general reduction in cloud cover in the FE scenario acts counter to the direct cooling of the aerosol, largely cancelling out any net impact on the RB.

There are only major differences to $SW^{\downarrow}_{Sfc}$ and RB between the 5 and 1 km domains on the 18 September case study because there is limited cloud cover and precipitation over the 1 km domain region on the other two case studies. In the 1 km domain, convection initiates faster and more energetically in the early afternoon compared to the same runs on the 5 km domain. Clouds are better resolved, covering a smaller portion of the total domain. Therefore, a greater amount of SW radiation reaches the ground in the 1 km domain compared to the same region of the 5 km domain (Fig. 7a). Over 24 h, approximately 18 $W m^{-2}$ more SW radiation reaches the surface in the Ctrl scenario in the 1 km domain compared to the same region of the 5 km domain. Assuming the representation of convective clouds is more realistic in the 1 km domain, the difference between the two domains could be an indication that the Grell-3-D parameterisation, even with subsistence spreading, is not suitable for predicting the semi-direct effect at this resolution. Note "suitability" here is only in regard to the simulation of the semi-direct effect. The convective parameterisation may still improve the model performance under other metrics, such as precipitation.

ACPD
15, 27449–27499, 2015

4.3 Sensitivity to convective parameterisation

To separate changes due to the aerosol fields from effects due to the convective parameterisation, a set of four scenarios without the Grell-3-D convective parameterisation over the 5 km domain were run for the 18 September case study. Total cloud cover is marginally reduced in the local afternoon without the convective parameterisation. However, the clearest effect is that there is a large reduction in ice clouds at night (Fig. 8). Deep convective towers are smaller and take longer to form without a convective parameterisation, delaying the onset of and reducing total precipitation. The FE_nCU scenario has slightly increased precipitation at night compared to nFE_nCU, whereas the FE scenario has less precipitation over the entire day compared to nFE (Fig. 8c).

The runs without convective parameterisation have reduced deep convection in the local afternoon, resulting in more downwelling SW radiation at the surface (Fig. 9a). The change in surface SW radiation at local afternoon is approximately twice as sensitive to the use of convective parameterisation to the presence of BBA. The reduction of high-altitude nighttime ice clouds when running without the convective parameterisation creates an extremely strong negative forcing at night as more LW radiation is lost to space in the runs without convective parameterisation (Fig. 9b). Overall, RB is more sensitive to whether or not a convective parameterisation is used than it is to the presence of aerosol or the horizontal resolution, with diurnally averaged reduction of approximately 20 $W m^{-2}$ between scenarios with and without convective parameterisation (Table S2 in the Supplement). This change is largely due to the reduction in nighttime clouds in the runs without convective parameterisation.

Changes in cloud cover due to the presence of aerosol have a smaller impact on the net radiative balance on the 1 km domain, resulting in lower magnitude of changes to the radiative budget (Fig. 10). The 1 km domain is sensitive to the boundary conditions from the 5 km domain, highlighted by the similarity in nighttime radiative balance changes due to ice clouds between the 1 km domain and same region covered by the

ACPD
15, 27449–27499, 2015

5 km domain (Fig. 10a and b). Precipitation is strongly suppressed over the 1 km region in the 5 km domain in the scenarios where convective parameterisation is turned off (Fig. 10c and d). More precipitation is produced in the 1 km domain for these runs, although still less than in the scenarios with convective parameterisation over the 5 km domain, highlighting the importance of the boundary conditions from the 5 km in determining the behaviour of the 1 km domain. In contrast, the runs with convective parameterisation turned on produce similar amounts of precipitation at both resolutions, implying that a convective parameterisation is needed over the 5 km domain to produce reasonable levels of precipitation.

4.4 Evidence of aerosol–cloud interactions

To show that BBA are activating to become cloud droplets in the model, we estimate the maximum supersaturation S_{max} in each column of the model with cloud by comparing the maximum droplet number in a vertical column ($N_{d,\,max}$) with the CCN concentrations at the base of the cloud. For example, if $N_{d,\,max} > CCN_{0.02}$ but $N_{d,\,max} < CCN_{0.1}$, then S_{max} must be between 0.02 and 0.1 %. This approach implicitly assumes that peak S_{max} is at cloud-base, which is a reasonable assumption given the representation by the Abdul-Razzak and Ghan (2002) activation parameterisation, but not in a parcel model or reality. Figures 11 and 12 show an increase in $N_{d,\,max}$ and corresponding decrease in S_{max} in the FE scenario, consistent with increased CCN activation.

Because the Abdul-Razzak and Ghan (2002) parameterisation estimates the activated fraction based on a Gaussian distribution of the updraft velocity (w), $N_{d,\,max}$ and S_{max} are both implicitly sensitive to w. However, most clouds over this period and region were convective and parameterised on the 5 km domain, meaning the subgrid variation vertical velocities is unresolved. To identify any aerosol–cloud interactions in convective systems, simulations at cloud resolving scales must be run. Comparing clouds in the same region of the 5 km and 1 km domain, S_{max} and $N_{d,\,max}$ are both approximately twice as high in the 1 km simulations in both FE and nFE scenarios, but clouds are smaller with less horizontal spread (Fig. 12). More CCN per unit volume are

ACPD
15, 27449–27499, 2015

activated in the 1 km domain due to *w* being explicitly resolved. However, there is no corresponding increase in scattered radiation, as may be expected from the first indirect effect, because deep convective clouds are already optically thick. Cloud optical depth is most sensitive to an increase in droplet number if the liquid water path is low (Twomey, 1974).

Although CCN are activated in cloud within the model, the net radiative balance was largely not sensitive to aerosol–cloud interactions during the case studies. In Fig. 5d to f, the nARI scenario, with full fire emissions but no aerosol–radiation interactions, closely follows the Ctrl simulation, indicating that the aerosol–cloud interactions by themselves have little impact on the radiative budget. An exception is on the morning of 23 September 2012 between 11:00 and 14:00 UTC, when there is enhanced cooling in both the FE and nARI scenarios (Fig. 5c). The large central region in Fig. 11a shows high droplet number in the FE scenario, whereas there is little cloud over the same region of the nFE run (Fig. 11c). This cloud is a ground-level radiation fog, which forms in the high morning humidity of the forest and is enhanced by the added presence of CCN from BBA. This example is the only period of the case studies where BBA aerosol influences the optical properties of resolved clouds in the 5 km domain, simulating the first indirect effect and reducing downwelling SW radiation.

5 Conclusions

WRF-Chem model simulations for three case studies over nested 5 and 1 km nested domains were conducted over a region of Brazil heavily influenced by biomass burning aerosol (BBA) to evaluate the regional impact of aerosol–radiation and aerosol–cloud interactions. The nested domains were driven by model fields from a WRF-Chem simulation at 25 km horizontal grid spacing over South America, which was run for September 2012 and evaluated by Archer-Nicholls et al. (2015) against in-situ aircraft measurements. The Grell-3-D convective parameterisation was used on the 5 km domain, using the recommended subsistence spreading option for running at this scale

ACPD
15, 27449–27499, 2015

(Grell and Freitas, 2014). Different scenarios were conducted to probe how effectively the impacts are modelled in WRF-Chem and test sensitivity to model resolution and use of convective parameterisation over the 5 km domain.

The direct effects of BBA particles over the region have a negative instantaneous forcing at the top of the atmosphere, despite being radiatively absorbing, due to the aerosol layer being over a low albedo surface. There is a strong cooling at the surface coupled with a warming in the lower troposphere, stabilising the atmospheric column and driving a semi-direct warming effect whereby the presence of aerosol inhibits cloud formation, reduces cloud cover and increases the amount of solar radiation reaching the ground. This result is similar to findings by, for example, Zhang et al. (2008) who find that the semi-direct effect in this region tends to be positive, partially or completely cancelling out the negative direct forcing.

Further nested simulations at 1 km grid spacing were run to explicitly resolve convection. In the finer resolution domain, deep convective clouds have much reduced horizontal spread but higher cloud droplet number within cloud compared to the 5 km domain. The reduction in cloud cover due to the presence of BBA over the 1 km domain therefore has a reduced impact on the net radiative balance and the magnitude of the semi-direct effect is smaller compared to the 5 km domain. The modelled semi-direct effect is thus highly sensitive to the model resolution. Any changes to the radiative balance due to aerosol–cloud interactions in the 1 km domain are masked by this reduction of the semi-direct effect. WRF-Chem (at the time of study) neglects fractional cloud cover within grid cells (Zhang, 2008), which may be causing an overestimation of a semi-direct effect over the 5 km domain. A better representation of fractional cloud cover, linked with the radiation and convective parameterisations, is likely needed to better evaluate this forcing at the regional scale.

Simulations run without a convective parameterisation on the 5 km domain had reduced daytime convection and precipitation, indicating some parameterised cloud is likely needed at this scale to produce reasonable precipitation. Turning off the convective parameterisation reduces ice cloud cover over night, allowing more LW radiation

ACPD
15, 27449–27499, 2015

to escape resulting in a negative instantaneous forcing of around $-50\,W\,m^{-2}$. While this result may be of little practical significance, the large magnitude of the sensitivity highlights the uncertainties with simulating aerosol–radiation–cloud interactions in this regime.

There was evidence that BBA CCN efficiently activate in the region, modelled as an increase in droplet number and decrease in maximum supersaturation in clouds. With the exception of an enhanced fog formation event on the morning of 23 September, aerosol–cloud interactions did not cause a noticeable change to the radiative balance. However, there are no aerosol–cloud interactions in parameterised clouds within WRF-Chem v3.4.1 used in this study. More CCN are activated in deep convective clouds in runs with fire emissions and convective parameterisation on, but without resolving the high in-cloud updraft velocities the physical significance of the modelled droplet number and grid-scale cloud properties of parameterised cloud is questionable. The runs with explicitly resolved convection at 1 km and no cumulus parameterisation at 5 km also showed minimal indirect effects, likely due to the deep convective clouds being optically thick and therefor not sensitive to increased droplet number. The model does not produce an aerosol "cloud-invigoration" effect, as described by Rosenfeld et al. (2008), both in simulations with and without a convective parameterisation. However, this may be because aerosol-ice nucleation processes are required to reproduce this effect. Overall, we find the semi-direct effect has a much greater impact on the net radiative balance than any indirect effects.

This case study investigation uses relatively short model simulations that do not have time to fully adjust to the aerosol forcings. The short runs also result in many of the results not being statistically significant according to Student *t* test criteria or similar, owing to a limited number of independent data points. The innermost 1 km domain would also benefit from being larger so as to be more consistently representative of the 5 km domain. A more robust estimate of the aerosol forcings would require long term simulations over multiple months. The high computational expense of running with sufficiently high resolution to resolve the effects investigated in this study would

ACPD
15, 27449–27499, 2015

be considered when undertaking studies for this purpose. The shorter case-studies at high-resolution were prioritised over a longer, low-resolution setup for the purpose and scope of the current investigation.

Simulating convective systems with the effects of aerosol included, particularly at horizontal grid spacings of less than 10 km, is a challenging task and work is being conducted to develop new parameterisations for this purpose (e.g. Grell and Freitas, 2014; Berg et al., 2014). The semi-direct effects are impossible to quantify reliably in this WRF-Chem setup due to this high sensitivity to the use of convective parameterisation and model resolution. More coordinated development of convective parameterisations with aerosol and radiation mechanisms is needed to have more certainty of these impacts and produce reasonable quantitative estimates. Without a consistent methodology for simulating aerosol–radiation–cloud interactions across scales, it is impossible to be sure how much of an impact the aerosol should be having on cloud properties and lifetime.

Appendix A: Calculating the radiative effects of an aerosol layer over WRF-Chem domains

The following is a description of the calculations used to evaluate the changes to the radiative balance due to the aerosol layer. It is related to and builds on other studies, such as Zhang et al. (2014), but includes to the changes to the long-wave (LW) as well as short-wave (SW) spectrum. WRF-Chem provides a set of 16 diagnostic variables for assessing simulated radiative fluxes, all given in units of $\mathrm{W\,m^{-2}}$. These are first split into SW and LW portions of the spectrum, and can be calculated at the top of the atmosphere (TOA) or at ground level (e.g. $\mathrm{SW_{TOA}}$ or $\mathrm{SW_{Sfc}}$ respectively) in either the up or down direction ($\mathrm{SW^{\uparrow}_{TOA}}$ or $\mathrm{SW^{\downarrow}_{TOA}}$). Finally, they can be calculated for "all-sky", including the effects of clouds ($\mathrm{SW^{\uparrow}_{TOA}}$); or for "clear-sky", ignoring the effects of clouds ($\mathrm{SW^{\uparrow}_{TOA,clr}}$). Note that the clear-sky variables are not only calculated in the grid points

ACPD
15, 27449–27499, 2015

where there is no cloud, but rather for every grid point giving the value that would be returned if no cloud existed.

The change to any of these variables due to the aerosol layer can be calculated by finding the difference between the FE scenario and a control scenario. For example, the change in downward SW radiation at the surface can be found by:

$$\Delta SW^{\downarrow}_{Sfc,FE} = SW^{\downarrow}_{Sfc,FE} - SW^{\downarrow}_{Sfc,Ctrl}. \quad (A1)$$

The radiative balance (RB) is defined as the difference between the radiation going into the system and the out-welling radiation at the TOA:

$$RB = SW^{\downarrow}_{TOA} + LW^{\downarrow}_{TOA} - SW^{\uparrow}_{TOA} - LW^{\uparrow}_{TOA}, \quad (A2)$$

with a positive RB indicating a net increase in energy in the system. As such, the RB is generally positive during the day and negative at night. RB can similarly be calculated for clear-sky conditions:

$$RB_{clr} = SW^{\downarrow}_{TOA,clr} + LW^{\downarrow}_{TOA,clr} - SW^{\uparrow}_{TOA,clr} - LW^{\uparrow}_{TOA,clr}. \quad (A3)$$

The change to the radiative balance due to clouds can then be inferred as the difference between the total radiative balance and the clear-sky case:

$$RB_{cld} = RB - RB_{clr}. \quad (A4)$$

The change in radiative balance (ΔRB) is defined as the difference between a particular scenario and the control simulation (Ctrl) which has no aerosol effects. Given the incoming radiation at TOA is the same for all scenarios, ΔRB is equal to the difference in outgoing radiation. For example for the fire emissions (FE) scenario:

$$\Delta RB_{FE} = RB_{FE} - RB_{Ctrl} = (SW^{\uparrow}_{TOA} + LW^{\uparrow}_{TOA})|_{Ctrl} - (SW^{\uparrow}_{TOA} + LW^{\uparrow}_{TOA})|_{FE}, \quad (A5)$$

ACPD
15, 27449–27499, 2015

making ΔRB_{FE} the instantaneous change to the net radiative flux due to the aerosol population. Similar calculations can be made for the clear-sky and cloud-only variables to separate the direct aerosol effects from changes to the cloud fields:

$$\Delta RB_{FE,clr} = RB_{FE,clr} - RB_{Ctrl,\,clr}; \qquad \Delta RB_{FE,cld} = RB_{FE,cld} - RB_{Ctl,\,cld}. \tag{A6}$$

The clear-sky variable $\Delta RB_{FE,clr}$ is somewhat equivalent to the instantaneous forcing due to aerosol–radiation interactions (RF_{ari}) as defined by the IPCC (IPCC, 2013), whereas ΔRB_{FE} gives an indication of the effective radiative forcing with aerosol–radiation aerosol–cloud interactions, after short-term adjustments ($ERF_{ari+aci}$). However, given the limited spatial and temporal scope of the study and the fact that large scale circulation is unaffected, these calculations should not be seen as robust calculations of the radiative forcing.

BBA contains a high proportion of highly absorbing black carbon. The total radiative flux absorbed by the atmosphere can be calculated by finding the difference between fluxes into and out of the atmospheric column. For example, for SW radiation:

$$ASW = SW^{\downarrow}_{TOA} + SW^{\uparrow}_{Sfc} - SW^{\uparrow}_{TOA} - SW^{\downarrow}_{Sfc}. \tag{A7}$$

For all derived radiative variables defined in this appendix, the average effect over a domain can given by calculating a mean across the domain, as well as over a period of time, whilst a measure of the spatial variation can be given by the standard deviation.

The Supplement related to this article is available online at doi:10.5194/acpd-15-27449-2015-supplement.

Acknowledgements. This work was funded by the Natural Environment Research Council (NERC) as part of the SAMBBA project under grant NE/J010073/1. S. Archer-Nicholls was supported by a NERC quota studentship, with partial support from NERC grant NE/J009202/1. Model simulations were carried out on the ARCHER UK National Supercomputing Service (http://www.archer.ac.uk). Version 3.4.1 of the WRF-Chem model is available from http://www2.mmm.ucar.edu/wrf/users/download/get_source.html. The code modifications following

ACPD
15, 27449–27499, 2015

Archer-Nicholls et al. (2015) used in the current study can be obtained by contacting the corresponding author. We thank B. Johnson, S. Kolusu and J. Marsham for helpful discussions on the paper. Analysis and figures were generated using NCAR Command Language v6.1.2 (http://www.ncl.ucar.edu/). We thank the developers of example scripts and WRF-specific functions, which we have used and modified extensively to carry out the presented analysis.

References

Abdul-Razzak, H. and Ghan, S. J.: A parameterization of aerosol activation 2. multiple aerosol types, J. Geophys. Res., 105, 6837–6844, 2000. 27459

Abdul-Razzak, H. and Ghan, S. J.: A parameterization of aerosol activation 3. sectional representation, J. Geophys. Res., 107, 4026, doi:10.1029/2001JD000483, 2002. 27458, 27459, 27468

Abdul-Razzak, H., Ghan, S. J., and Rivera-carpio, C.: A parameterization of aerosol activation: 1. single aerosol type, J. Geophys. Res., 103, 6123–6131, 1998.

Ackerman, A. S., Toon, O. B., Stevens, D. E., Heymsfield, A. J., Ramanathan, V., and Welton, E. J.: Reduction of tropical cloudiness by soot, Science, 288, 1042–1047, doi:10.1126/science.288.5468.1042, 2000. 27451

Allen, R. J. and Sherwood, S. C.: Aerosol-cloud semi-direct effect and land–sea temperature contrast in a GCM, Geophys. Res. Lett., 37, L07702, doi:10.1029/2010GL042759, 2010. 27451

Andreae, M. O. and Rosenfeld, D.: Aerosol–cloud–precipitation interactions, Part 1. The nature and sources of cloud-active aerosols, Earth-Sci. Rev., 89, 13–41, doi:10.1016/j.earscirev.2008.03.001, 2008. 27452

Andreae, M. O., Rosenfeld, D., Artaxo, P., Costa, A. A., Frank, G. P., Longo, K. M., and Silva-Dias, M. A. F.: Smoking rain clouds over the Amazon, Science, 303, 1337–1342, doi:10.1126/science.1092779, 2004. 27451

Archer-Nicholls, S., Lowe, D., Darbyshire, E., Morgan, W. T., Bela, M. M., Pereira, G., Trembath, J., Kaiser, J. W., Longo, K. M., Freitas, S. R., Coe, H., and McFiggans, G.: Characterising Brazilian biomass burning emissions using WRF-Chem with MOSAIC sectional aerosol, Geosci. Model Dev., 8, 549–577, doi:10.5194/gmd-8-549-2015, 2015. 27454, 27455, 27456, 27460, 27461, 27463, 27469, 27475

ACPD
15, 27449–27499, 2015

Baklanov, A., Mahura, A., and Sokhi, R. S. (Eds.): Integrated Systems of Meso-Meteorological and Chemical Transport Models, Springer-Verlag, Berlin, Heidelberg, doi:10.1007/978-3-642-13980-2, 2011. 27452

Baklanov, A., Schluenzen, K. H., Suppan, P., Baldasano, J., Brunner, D., Aksoyoglu, S., Carmichael, G., Douros, J., Flemming, J., Forkel, R., Galmarini, S., Gauss, M., Grell, G., Hirtl, M., Joffre, S., Jorba, O., Kaas, E., Kaasik, M., Kallos, G., Kong, X., Korsholm, U., Kurganskiy, A., Kushta, J., Lohmann, U., Mahura, A., Manders-Groot, A., Maurizi, A., Moussiopoulos, N., Rao, S. T., Savage, N., Seigneur, C., Sokhi, R., Solazzo, E., Solomos, S., Sørensen, B., Tsegas, G., Vignati, E., Vogel, B., and Zhang, Y.: Online coupled regional meteorology-chemistry models in Europe: current status and prospects, Atmos. Chem. Phys. Discuss., 13, 12541–12724, doi:10.5194/acpd-13-12541-2013, 2013. 27452

Barnard, J. C., Fast, J. D., Paredes-Miranda, G., Arnott, W. P., and Laskin, A.: Technical Note: Evaluation of the WRF-Chem "Aerosol Chemical to Aerosol Optical Properties" Module using data from the MILAGRO campaign, Atmos. Chem. Phys., 10, 7325–7340, doi:10.5194/acp-10-7325-2010, 2010. 27453, 27457, 27458

Berg, L. K., Shrivastava, M., Easter, R. C., Fast, J. D., Chapman, E. G., and Liu, Y.: A new WRF-Chem treatment for studying regional scale impacts of cloud-aerosol interactions in parameterized cumuli, Geosci. Model Dev. Discuss., 7, 2651–2704, doi:10.5194/gmdd-7-2651-2014, 2014. 27460, 27472

Bohren, C. Z. and Huffman, D. R.: Absorption and Scattering of Light by Small Particles, Wiley, New York, USA, 1983. 27457

Bond, T. C. and Bergstrom, R. W.: Light absorption by carbonaceous particles: an investigative review, Aerosol Sci. Tech., 39, 1–41, doi:10.1080/02786820500421521, 2006. 27457, 27458

Bond, T. C., Habib, G., and Bergstrom, R. W.: Limitations in the enhancement of visible light absorption due to mixing state, J. Geophys. Res., 111, D20211, doi:10.1029/2006JD007315, 2006. 27457

Bond, T. C., Doherty, S. J., Fahey, D. W., Forster, P. M., Berntsen, T., Deangelo, B. J., Flanner, M. G., Ghan, S., Koch, D., Kinne, S., Kondo, Y., Quinn, P. K., Sarofim, M. C., Schultz, M. G., Schulz, M., Zhang, H., Zhang, S., Bellouin, N., Guttikunda, S. K., Hopke, P. K., Jacobson, M. Z., Klimont, Z., Lohmann, U., Schwarz, J. P., Shindell, D., Storelvmo, T., Warren, S. G., and Zender, C. S.: Bounding the role of black carbon in the climate system: a scientific assessment, J. Geophys. Res.-Atmos., 11, 1–163, 2013. 27451

ACPD
15, 27449–27499, 2015

Boucher, O., Randall, D., Artaxo, P., Bretherton, C., Feingold, G., Forster, P., Kerminen, V.-M., Kondo, Y., Liao, H., Lohmann, U., Rasch, P., Satheesh, S. K., Sherwood, S., Stevens, B., and Zhang, X. Y.: IPCC 2013, clouds and aerosols, in: Climate Change 2013: The Physical Science Basis, Contribution of Working Group I to the Fifth Assessment Report of the Intergovernmental Panel on Climate Change, edited by: Stocker, T. F., Qin, D., Plattner, G.-K., Tignor, M., Allen, S. K., Boschung, J., Nauels, A., Xia, Y., Bex, V., and Midgley, P. M., Cambridge University Press, Cambridge, UK and New York, NY, USA, 2013. 27451, 27452, 27474

Chapman, E. G., Gustafson Jr., W. I., Easter, R. C., Barnard, J. C., Ghan, S. J., Pekour, M. S., and Fast, J. D.: Coupling aerosol-cloud-radiative processes in the WRF-Chem model: Investigating the radiative impact of elevated point sources, Atmos. Chem. Phys., 9, 945–964, doi:10.5194/acp-9-945-2009, 2009. 27453, 27459, 27460

Chand, D., Wood, R., Anderson, T. L., Satheesh, S. K., and Charlson, R. J.: Satellite-derived direct radiative effect of aerosols dependent on cloud cover, Nat. Geosci., 2, 181–184, doi:10.1038/ngeo437, 2009. 27451

Chen, Y.-C., Xue, L., Lebo, Z. J., Wang, H., Rasmussen, R. M., and Seinfeld, J. H.: A comprehensive numerical study of aerosol-cloud-precipitation interactions in marine stratocumulus, Atmos. Chem. Phys., 11, 9749–9769, doi:10.5194/acp-11-9749-2011, 2011. 27452

Cook, J. and Highwood, E. J.: Climate response to tropospheric absorbing aerosols in an intermediate general-circulation model, Q. J. Roy. Meteor. Soc., 130, 175–191, doi:10.1256/qj.03.64, 2004. 27452

Donahue, N. M., Epstein, S. A., Pandis, S. N., and Robinson, A. L.: A two-dimensional volatility basis set: 1. organic-aerosol mixing thermodynamics, Atmos. Chem. Phys., 11, 3303–3318, doi:10.5194/acp-11-3303-2011, 2011. 27457

Fast, J. D., Gustafson, W. I., Easter, R. C., Zaveri, R. A., Barnard, J. C., Chapman, E. G., Grell, G. A., and Peckham, S. E.: Evolution of ozone, particulates, and aerosol direct radiative forcing in the vicinity of Houston using a fully coupled meteorology-chemistry-aerosol model, J. Geophys. Res., 111, 1–29, doi:10.1029/2005JD006721, 2006. 27453, 27456, 27458

Fast, J. D., Allan, J., Bahreini, R., Craven, J., Emmons, L., Ferrare, R., Hayes, P. L., Hodzic, A., Holloway, J., Hostetler, C., Jimenez, J. L., Jonsson, H., Liu, S., Liu, Y., Metcalf, A., Middlebrook, A., Nowak, J., Pekour, M., Perring, A., Russell, L., Sedlacek, A., Seinfeld, J., Setyan, A., Shilling, J., Shrivastava, M., Springston, S., Song, C., Subramanian, R., Taylor, J. W., Vinoj, V., Yang, Q., Zaveri, R. A., and Zhang, Q.: Modeling regional aerosol and

ACPD
15, 27449–27499, 2015

aerosol precursor variability over California and its sensitivity to emissions and long-range transport during the 2010 CalNex and CARES campaigns, Atmos. Chem. Phys., 14, 10013–10060, doi:10.5194/acp-14-10013-2014, 2014. 27453

Flemming, J., Peuch, V.-H., Engelen, R., and Kaiser, J. W.: A European global-to-regional air pollution forecasting system that combines modeling with satellite observations, EM Magazine, November 2013, 6–10, 2013. 27460

Freitas, S. R., Longo, K. M., Chatfield, R., Latham, D., Silva Dias, M. A. F., Andreae, M. O., Prins, E., Santos, J. C., Gielow, R., and Carvalho Jr., J. A.: Including the sub-grid scale plume rise of vegetation fires in low resolution atmospheric transport models, Atmos. Chem. Phys., 7, 3385–3398, doi:10.5194/acp-7-3385-2007, 2007. 27455, 27461

Freitas, S. R., Longo, K. M., Alonso, M. F., Pirre, M., Marecal, V., Grell, G., Stockler, R., Mello, R. F., and Sánchez Gácita, M.: PREP-CHEM-SRC – 1.0: a preprocessor of trace gas and aerosol emission fields for regional and global atmospheric chemistry models, Geosci. Model Dev., 4, 419–433, doi:10.5194/gmd-4-419-2011, 2011. 27456

Ghan, S., Laulainen, N., Easter, R., Wagener, R., Nemesure, S., Chapman, E., Zhang, Y., and Leung, R.: Evaluation of aerosol direct radiative forcing in MIRAGE, J. Geophys. Res., 106, 5295–5316, 2001. 27458

Ghan, S. J. and Easter, R. C.: Impact of cloud-borne aerosol representation on aerosol direct and indirect effects, Atmos. Chem. Phys., 6, 4163–4174, doi:10.5194/acp-6-4163-2006, 2006. 27452

Ghan, S. J., Leung, L. R., Easter, R. C., and Abdul-Razzak, H.: Prediction of cloud droplet number in a general circulation model, J. Geophys. Res., 102, 21777–21794, 1997. 27459

Grell, G. and Baklanov, A.: Integrated modeling for forecasting weather and air quality: a call for fully coupled approaches, Atmos. Environ., 45, 6845–6851, doi:10.1016/j.atmosenv.2011.01.017, 2011. 27453

Grell, G. A. and Freitas, S. R.: A scale and aerosol aware stochastic convective parameterization for weather and air quality modeling, Atmos. Chem. Phys., 14, 5233–5250, doi:10.5194/acp-14-5233-2014, 2014. 27453, 27460, 27461, 27470, 27472

Grell, G. A., Peckham, S. E., Schmitz, R., McKeen, S. A., Frost, G., Skamarock, W. C., and Eder, B.: Fully coupled "online" chemistry within the WRF model, Atmos. Environ., 39, 6957–6975, doi:10.1016/j.atmosenv.2005.04.027, 2005. 27453, 27456

ACPD
15, 27449–27499, 2015

Grell, G., Freitas, S. R., Stuefer, M., and Fast, J.: Inclusion of biomass burning in WRF-Chem: impact of wildfires on weather forecasts, Atmos. Chem. Phys., 11, 5289–5303, doi:10.5194/acp-11-5289-2011, 2011. 27453, 27454

Guenther, A., Karl, T., Harley, P., Wiedinmyer, C., Palmer, P. I., and Geron, C.: Estimates of global terrestrial isoprene emissions using MEGAN (Model of Emissions of Gases and Aerosols from Nature), Atmos. Chem. Phys., 6, 3181–3210, doi:10.5194/acp-6-3181-2006, 2006.

Hansen, J., Sato, M., and Ruedy, R.: Radiative forcing and climate response, J. Geophys. Res., 102, 6831–6864, 1997. 27451

Haywood, J. and Boucher, O.: Estimates of the direct and indirect radiative forcing due to tropospheric aerosols: a review, Rev. Geophys., 38, 513, doi:10.1029/1999RG000078, 2000. 27451

Haywood, J. M. and Shine, K. P.: The effect of anthropogenic sulfate and soot aerosol on the clear sky planetary radiation budget, Geophys. Res. Lett., 22, 603–606, 1995. 27451

Hennigan, C. J., Westervelt, D. M., Riipinen, I., Engelhart, G. J., Lee, T., Collett, J. L., Pandis, S. N., Adams, P. J., and Robinson, A. L.: New particle formation and growth in biomass burning plumes: an important source of cloud condensation nuclei, Geophys. Res. Lett., 39, L09805, doi:10.1029/2012GL050930, 2012. 27451

Hollingsworth, A., Engelen, R. J., Benedetti, A., Dethof, A., Flemming, J., Kaiser, J. W., Morcrette, J.-J., Simmons, a. J., Textor, C., Boucher, O., Chevallier, F., Rayner, P., Elbern, H., Eskes, H., Granier, C., Peuch, V.-H., Rouil, L., and Schultz, M. G.: Toward a monitoring and forecasting system for atmospheric composition: the GEMS project, B. Am. Meteorol. Soc., 89, 1147–1164, doi:10.1175/2008BAMS2355.1, 2008. 27460

Hong, S.-Y., and Dudhia, J.: Next-generation numerical weather prediction: bridging parameterization, explicit clouds, and large eddies, B. Am. Meteorol. Soc., 93, ES6–ES9, doi:10.1175/2011BAMS3224.1, 2012. 27453

Iacono, M. J., Mlawer, E. J., and Clough, S. A.: Impact of an improved longwave radiation model, RRTM, on the energy budget and thermodynamic properties of the NCAR community climate model, CCM3, J. Geophys. Res., 105, 14873–14890, 2000. 27458

Janhäll, S., Andreae, M. O., and Pöschl, U.: Biomass burning aerosol emissions from vegetation fires: particle number and mass emission factors and size distributions, Atmos. Chem. Phys., 10, 1427–1439, doi:10.5194/acp-10-1427-2010, 2010. 27459

ACPD
15, 27449–27499, 2015

Johnson, B. T.: The semidirect aerosol effect: comparison of a single-column model with large eddy simulation for marine stratocumulus, B. Am. Meteorol. Soc., 18, 119–130, 2004. 27452
Johnson, B. T., Shine, K. P., and Forster, P. M.: The semi-direct aerosol effect: impact of absorbing aerosols on marine stratocumulus, Q. J. Roy. Meteor. Soc., 130, 1407–1422, doi:10.1256/qj.03.61, 2004. 27451
Jolleys, M. D., Coe, H., McFiggans, G., Capes, G., Allan, J. D., Crosier, J., Williams, P. I., Allen, G., Bower, K. N., Jimenez, J. L., Russell, L. M., Grutter, M., and Baumgardner, D.: Characterizing the aging of biomass burning organic aerosol by use of mixing ratios: a meta-analysis of four regions, Environ. Sci. Technol., 46, 13093–13102, doi:10.1021/es302386v, 2012. 27457
Koch, D. and Del Genio, A. D.: Black carbon semi-direct effects on cloud cover: review and synthesis, Atmos. Chem. Phys., 10, 7685–7696, doi:10.5194/acp-10-7685-2010, 2010. 27451
Kodros, J. K., Scott, C. E., Farina, S. C., Lee, Y. H., L'Orange, C., Volckens, J., and Pierce, J. R.: Uncertainties in global aerosols and climate effects due to biofuel emissions, Atmos. Chem. Phys., 15, 8577–8596, doi:10.5194/acp-15-8577-2015, 2015. 27457
Köhler, H.: The nucleus in and the growth of hygroscopic droplets, T. Faraday Soc., 32, 1152–1161, doi:10.1039/TF9363201152, 1936. 27458
Kolusu, S. R., Marsham, J. H., Mulcahy, J., Johnson, B., Dunning, C., Bush, M., and Spracklen, D. V.: Impacts of Amazonia biomass burning aerosols assessed from short-range weather forecasts, Atmos. Chem. Phys. Discuss., 15, 18883–18919, doi:10.5194/acpd-15-18883-2015, 2015. 27464
Lohmann, U. and Feichter, J.: Global indirect aerosol effects: a review, Atmos. Chem. Phys., 5, 715–737, doi:10.5194/acp-5-715-2005, 2005. 27451
Lohmann, U. and Ferrachat, S.: Impact of parametric uncertainties on the present-day climate and on the anthropogenic aerosol effect, Atmos. Chem. Phys., 10, 11373–11383, doi:10.5194/acp-10-11373-2010, 2010. 27452
Longo, K. M., Freitas, S. R., Andreae, M. O., Setzer, A., Prins, E., and Artaxo, P.: The coupled aerosol and tracer transport model to the Brazilian developments on the regional atmospheric modeling system (CATT-BRAMS) – Part 2: Model sensitivity to the biomass burning inventories, Atmos. Chem. Phys., 10, 5785–5795, doi:10.5194/acp-10-5785-2010, 2010. 27456
Martin, S. T., Andreae, M. O., Artaxo, P., Baumgardner, D., Chen, Q., Goldstein, A. H., Guenther, A., Heald, C. L., Bracero, O. L. M., Mcmurry, P. H., Pauliquevis, T., Pöschl, U.,

ACPD
15, 27449–27499, 2015

Prather, K. A., Roberts, G. C., Saleska, S. R., Silva-Dias, M. A., Spracklen, D. V., and Swietlicki, E. T.: Sources and properties of amazonian aerosol particles, Rev. Geophys., 48, 1–42, doi:10.1029/2008RG000280, 2010. 27454

Matsui, H., Koike, M., Kondo, Y., Moteki, N., Fast, J. D., and Zaveri, R. A.: Development and validation of a black carbon mixing state resolved three-dimensional model: aging processes and radiative impact, J. Geophys. Res. Atmos., 118, 2304–2326, doi:10.1029/2012JD018446, 2013. 27457

McFiggans, G., Artaxo, P., Baltensperger, U., Coe, H., Facchini, M. C., Feingold, G., Fuzzi, S., Gysel, M., Laaksonen, A., Lohmann, U., Mentel, T. F., Murphy, D. M., O'Dowd, C. D., Snider, J. R., and Weingartner, E.: The effect of physical and chemical aerosol properties on warm cloud droplet activation, Atmos. Chem. Phys., 6, 2593–2649, doi:10.5194/acp-6-2593-2006, 2006. 27451, 27458

Mlawer, E. J., Taubman, S. J., Brown, P. D., Iacono, M. J., and Clough, S. A.: Radiative transfer for inhomogeneous atmospheres: RRTM, a validated correlated-k model for the longwave, J. Geophys. Res., 102, 16663–16682, doi:10.1029/97JD00237, 1997. 27458

Morrison, H., Curry, J. A., and Khvorostyanov, V. I.: A new double-moment microphysics parameterization for application in cloud and climate models, Part I: Description, J. Atmos. Sci., 62, 1665–1677, doi:10.1175/JAS3446.1, 2005. 27459

Morrison, H., Thompson, G., and Tatarskii, V.: Impact of cloud microphysics on the development of trailing stratiform precipitation in a simulated squall line: comparison of one- and two-moment schemes, Mon. Weather Rev., 137, 991–1007, doi:10.1175/2008MWR2556.1, 2009. 27459

Pöschl, U., Martin, S. T., Sinha, B., Chen, Q., Gunthe, S. S., Huffman, J. A, Borrmann, S., Farmer, D. K., Garland, R. M., Helas, G., Jimenez, J. L., King, S. M., Manzi, A, Mikhailov, E., Pauliquevis, T., Petters, M. D., Prenni, A. J., Roldin, P., Rose, D., Schneider, J., Su, H., Zorn, S. R., Artaxo, P., and Andreae, M. O.: Rainforest aerosols as biogenic nuclei of clouds and precipitation in the Amazon, Science, 329, 1513–1516, doi:10.1126/science.1191056, 2010. 27452

Possner, A., Zubler, E., Lohmann, U., and Schär, C.: Real-case simulations of aerosol–cloud interactions in ship tracks over the Bay of Biscay, Atmos. Chem. Phys., 15, 2185–2201, doi:10.5194/acp-15-2185-2015, 2015. 27451, 27452

ACPD
15, 27449–27499, 2015

Reid, J. S., Koppmann, R., Eck, T. F., and Eleuterio, D. P.: A review of biomass burning emissions part II: intensive physical properties of biomass burning particles, Atmos. Chem. Phys., 5, 799–825, doi:10.5194/acp-5-799-2005, 2005a. 27454

Reid, J. S., Eck, T. F., Christopher, S. A., Koppmann, R., Dubovik, O., Eleuterio, D. P., Holben, B. N., Reid, E. A., and Zhang, J.: A review of biomass burning emissions part III: intensive optical properties of biomass burning particles, Atmos. Chem. Phys., 5, 827–849, doi:10.5194/acp-5-827-2005, 2005b. 27454

Romakkaniemi, S., McFiggans, G., Bower, K. N., Brown, P., Coe, H., and Choularton, T. W.: A comparison between trajectory ensemble and adiabatic parcel modeled cloud properties and evaluation against airborne measurements, J. Geophys. Res.-Atmos., 114, D06214, doi:10.1029/2008JD011286, 2009. 27452

Rosenfeld, D., Lohmann, U., Raga, G. B., O'Dowd, C. D., Kulmala, M., Fuzzi, S., Reissell, A., and Andreae, M. O.: Flood or drought: how do aerosols affect precipitation?, Science, 321, 1309–13, doi:10.1126/science.1160606, 2008. 27451, 27452, 27471

Saide, P. E., Spak, S. N., Carmichael, G. R., Mena-Carrasco, M. A., Yang, Q., Howell, S., Leon, D. C., Snider, J. R., Bandy, A. R., Collett, J. L., Benedict, K. B., de Szoeke, S. P., Hawkins, L. N., Allen, G., Crawford, I., Crosier, J., and Springston, S. R.: Evaluating WRF-Chem aerosol indirect effects in Southeast Pacific marine stratocumulus during VOCALS-REx, Atmos. Chem. Phys., 12, 3045–3064, doi:10.5194/acp-12-3045-2012, 2012. 27453

Shrivastava, M., Fast, J., Easter, R., Gustafson Jr., W. I., Zaveri, R. A., Jimenez, J. L., Saide, P., and Hodzic, A.: Modeling organic aerosols in a megacity: comparison of simple and complex representations of the volatility basis set approach, Atmos. Chem. Phys., 11, 6639–6662, doi:10.5194/acp-11-6639-2011, 2011. 27457

Shrivastava, M., Berg, L. K., Fast, J. D., Easter, R. C., Laskin, A., Chapman, E. G., Jr, W. I. G., Liu, Y., and Berkowitz, C. M.: Modeling aerosols and their interactions with shallow cumuli during the 2007 CHAPS field study, J. Geophys. Res.-Atmos., 118, 1343–1360, doi:10.1029/2012JD018218, 2013. 27453, 27457

Simpson, E., Connolly, P., and McFiggans, G.: An investigation into the performance of four cloud droplet activation parameterisations, Geosci. Model Dev., 7, 1535–1542, doi:10.5194/gmd-7-1535-2014, 2014. 27459

Stein, O., Flemming, J., Inness, A., and Kaiser, J. W.: Global reactive gases forecasts and reanalysis in the MACC project, Journal of Integrative Environmental Sciences, 9, 1–14, doi:10.1080/1943815X.2012.696545, 2011.

ACPD
15, 27449–27499, 2015

Taylor, J. W., Allan, J. D., Allen, G., Coe, H., Williams, P. I., Flynn, M. J., Le Breton, M., Muller, J. B. A., Percival, C. J., Oram, D., Forster, G., Lee, J. D., Rickard, A. R., and Palmer, P. I.: Size-dependent wet removal of black carbon in Canadian biomass burning plumes, Atmos. Chem. Phys. Discuss., 14, 19469–19513, doi:10.5194/acpd-14-19469-2014, 2014.

Twomey, S.: Pollution and the planetary albedo, Atmos. Environ., 8, 1251–1256, 1974. 27451, 27469

Wu, L., Su, H., and Jiang, J. H.: Regional simulations of deep convection and biomass burning over South America: 1. model evaluations using multiple satellite data sets, J. Geophys. Res., 116, D17208, doi:10.1029/2011JD016106, 2011a. 27453

Wu, L., Su, H., and Jiang, J. H.: Regional simulations of deep convection and biomass burning over South America: 2. biomass burning aerosol effects on clouds and precipitation, J. Geophys. Res., 116, D17209, doi:10.1029/2011JD016106, 2011b. 27453, 27454

Yang, Q., W. I. Gustafson Jr., Fast, J. D., Wang, H., Easter, R. C., Morrison, H., Lee, Y.-N., Chapman, E. G., Spak, S. N., and Mena-Carrasco, M. A.: Assessing regional scale predictions of aerosols, marine stratocumulus, and their interactions during VOCALS-REx using WRF-Chem, Atmos. Chem. Phys., 11, 11951–11975, doi:10.5194/acp-11-11951-2011, 2011. 27453, 27459, 27460

Zaveri, R. A. and Peters, L. K.: A new lumped structure photochemical mechanism for large-scale applications, J. Geophys. Res., 104, 30387–30415, 1999. 27456

Zaveri, R. A., Easter, R. C., Fast, J. D., and Peters, L. K.: Model for simulating aerosol interactions and chemistry (MOSAIC), J. Geophys. Res., 113, D132024, doi:10.1029/2007JD008782, 2008. 27456

Zhang, F., Wang, J., Ichoku, C., Hyer, E. J., Yang, Z., Ge, C., Su, S., Zhang, X., Kondragunta, S., Kaiser, J. W., Wiedinmyer, C., and da Silva, A.: Sensitivity of mesoscale modeling of smoke direct radiative effect to the emission inventory: a case study in northern sub-Saharan African region, Environ. Res. Lett., 9, 075002, doi:10.1088/1748-9326/9/7/075002, 2014. 27454, 27472

Zhang, Y.: Online-coupled meteorology and chemistry models: history, current status, and outlook, Atmos. Chem. Phys., 8, 2895–2932, doi:10.5194/acp-8-2895-2008, 2008. 27470

Zhang, Y., Fu, R., Yu, H., Dickinson, R. E., Juarez, R. N., Chin, M., and Wang, H.: A regional climate model study of how biomass burning aerosol impacts land–atmosphere in-

ACPD
15, 27449–27499, 2015

teractions over the Amazon, J. Geophys. Res., 113, D14S15, doi:10.1029/2007JD009449, 2008. 27451, 27470

Zhao, C., Liu, X., Ruby Leung, L., and Hagos, S.: Radiative impact of mineral dust on monsoon precipitation variability over West Africa, Atmos. Chem. Phys., 11, 1879–1893, doi:10.5194/acp-11-1879-2011, 2011. 27453, 27458

ACPD

15, 27449–27499, 2015

Table 1. 8 bin MOSAIC size grid.

Bin number	particle dry diameter (nm)
1	39.0625–78.125
2	78.125–156.25
3	156.25–312.5
4	312.5–625
5	625–1250
6	1250–2500
7	2500–5000
8	5000–10 000

ACPD
15, 27449–27499, 2015

Table 2. Summary of physical parameterisations and other options used in parent and nested simulations.

Option	d01, 25 km parent	d02, 5 km nest	d03, 1 km nest
Horizontal Grid Cells ($n_i \times n_j$)	226 × 196	151 × 171	141 × 116
Horizontal grid spacing	25 km	5 km	1 km
Cumulus	Grell 3-D	Grell 3-D	None
Subsistance spreading	1	3	NA
Dynamical timestep (s)	120	30	6
Chemistry time-step (min)	2	1	1
Boundary conditions	ECMWF/MACC	offline, ndown	online, no feedback

ACPD
15, 27449–27499, 2015

Table 3. Summary of scenarios: fire Emissions (FE), no Fire Emissions (nFE), fire emissions with no Aerosol–Radiation Interactions (nARI), and a Control simulation with no fire emissions or aerosol–radiation interactions (Ctrl). Scenrios without convective parameterisation on the 5 km domain (FE_nCU, nFE_nCU, nARI_nCU and Ctrl_nCU) were run only for the 18 September case study.

Scenario	Fire emissions	Aerosol–radiative feedback	Convective parameterisation on 5 km domain
FE	On	On	On
nFE	Off	On	On
nARI	On	Off	On
Ctrl	Off	Off	On
FE_nCU	On	On	Off
nFE_nCU	Off	On	Off
nARI_nCU	On	Off	Off
Ctrl_nCU	Off	Off	Off

ACPD
15, 27449–27499, 2015

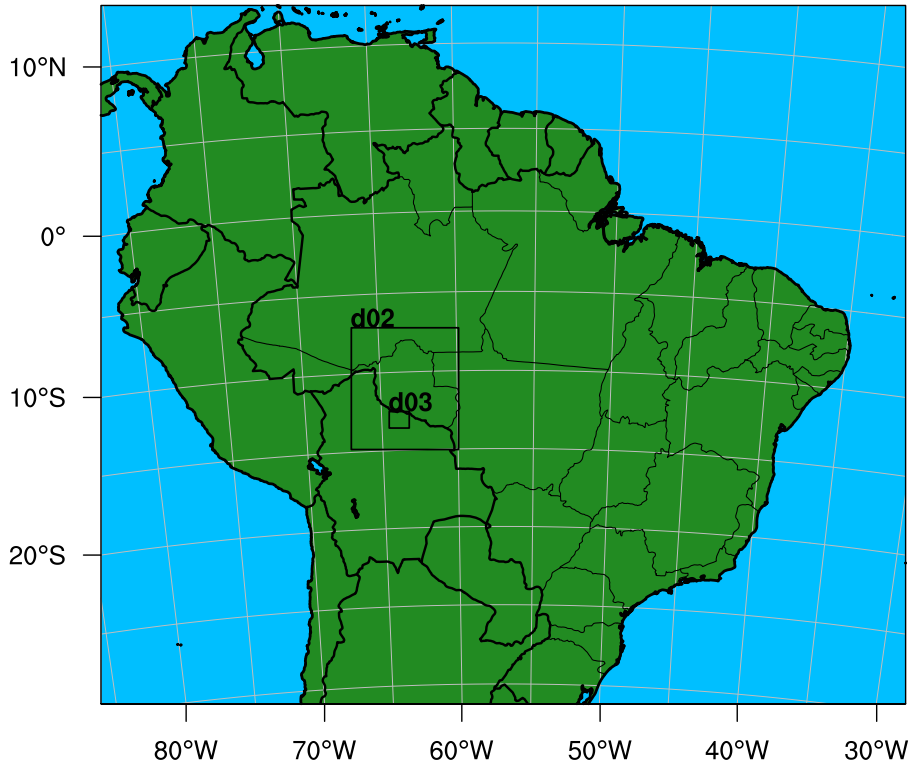

Figure 1. Map of domains used for study. Outer map of parent domain with 25 km horizontal grid spacing, with squares showing extents of 5 km (d02) and 1 km (d03) nests.

ACPD
15, 27449–27499, 2015

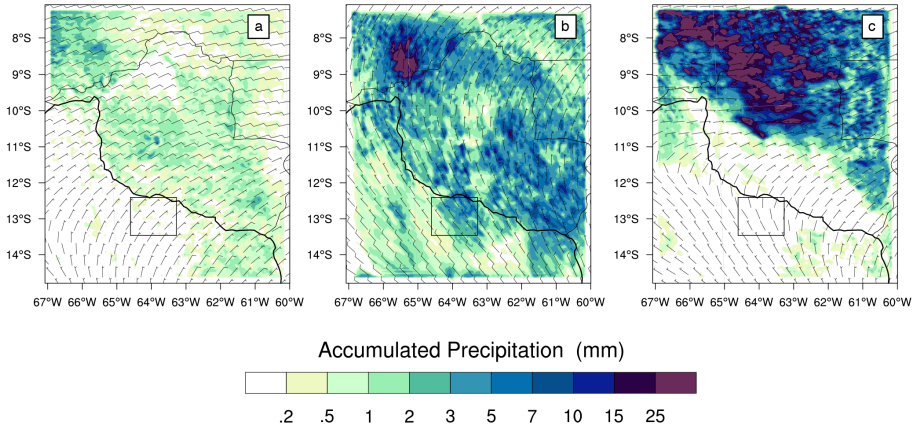

Figure 2. Maps of total precipitation and wind vectors at 700 hPa from the Ctrl scenario, averaged over 24 h from dawn to dawn for each case study period over the 5 km domain, with black box outlining the 1 km domain. **(a)** from 10:00 UTC 14 September, **(b)** from 10:00 UTC 18 September 2012; and **(c)** from 10:00 UTC 23 September.

ACPD
15, 27449–27499, 2015

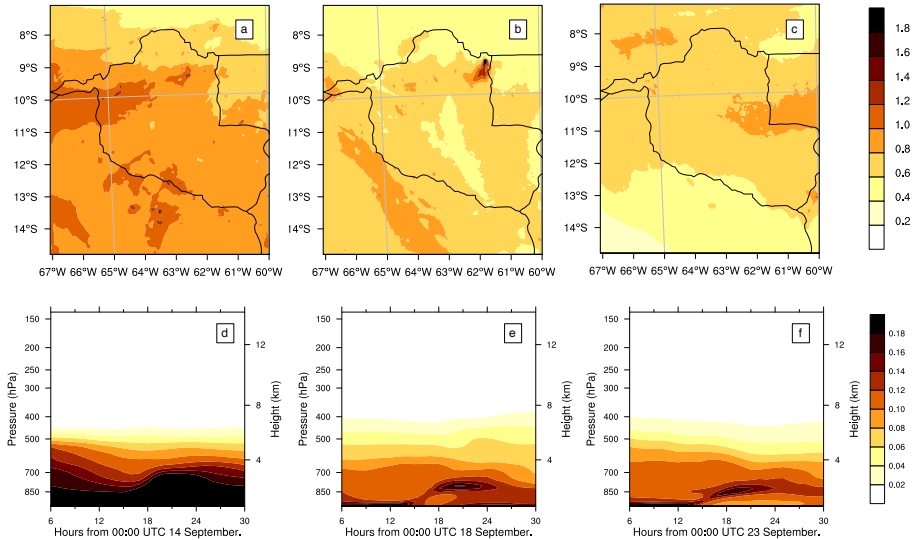

Figure 3. (a–c) Temporally averaged horizontal maps of column AOD at 550 nm from 5 km domain. **(d–f)** Vertical profiles of extinction coefficient b_{ext} at 550 nm (km^{-1}), averaged over interpolated pressure level planes at 25 hPa intervals. All data from FE scenario, **(a)** and **(d)** from 06:00 UTC 14 September; **(b)** and **(e)** from 06:00 UTC 18 September; **(c)** and **(f)** from 06:00 UTC 23 September 2012.

ACPD
15, 27449–27499, 2015

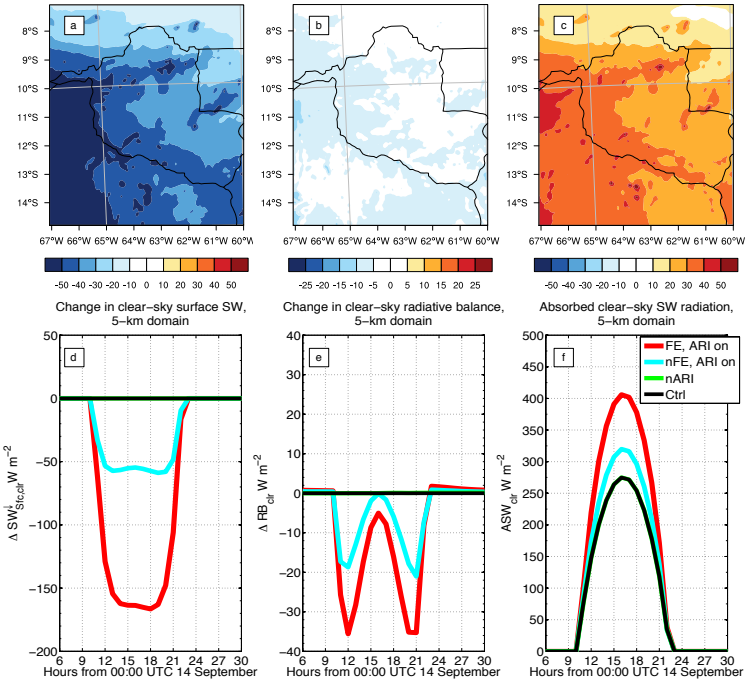

Figure 4. Maps and time-series of changes to clear-sky radiation fields (ignoring the effects of clouds) due to BBA over 14 September 2012. **(a–c)** show maps over 5 km domain of the difference between the FE and nFE scenarios, averaged over 24 h, from dawn to dawn, between 10:00 UTC 14 and 10:00 UTC 15 September. **(d–f)** show model output averaged over the 5 km domain at each hour of simulation for the FE, nFE, nARI and Ctrl scenarios; with **(d)** and **(e)** plotting difference from Ctrl scenario. **(a)** and **(d)** change in downwelling SW radiation at the surface $\Delta SW^{\downarrow}_{Sfc,\,clr}$. **(b)** and **(e)** change in radiative balance (ΔRB_{clr}) at top of the atmosphere (TOA). **(c)** and **(f)** SW radiation absorbed by the atmospheric column (ASW_{clr}). Calculations of derived variables are explained in AppendixA. All variables are in units $W\,m^{-2}$.

ACPD
15, 27449–27499, 2015

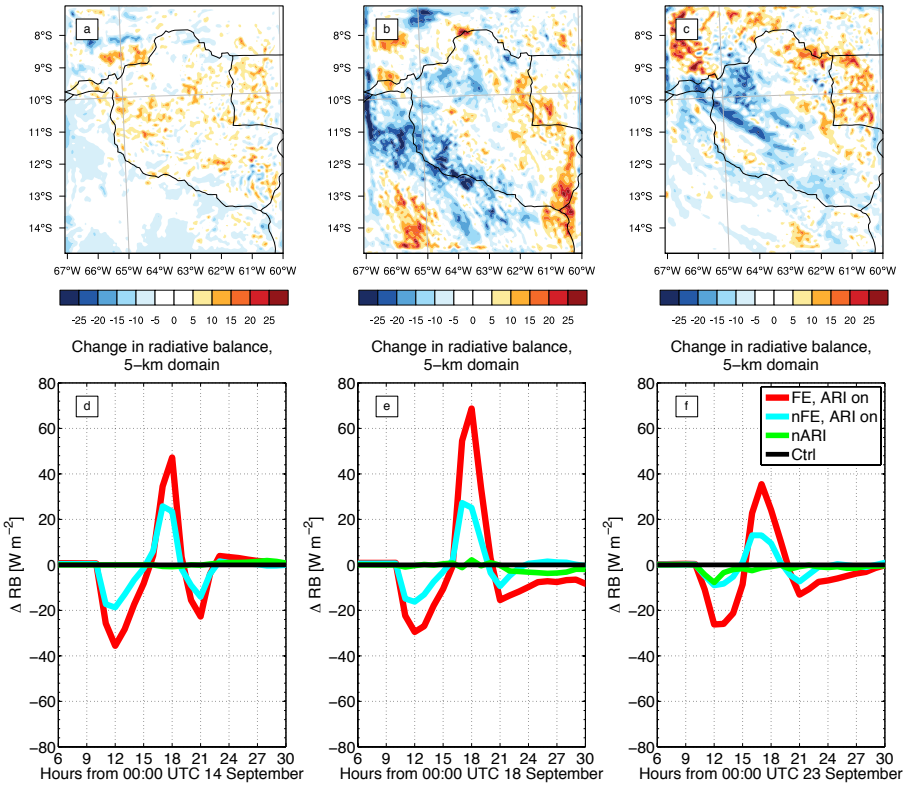

Figure 5. Changes to radiation balance at TOA over the 5 km domain for each of the three case study days, including the effects of clouds. **(a–c)** show maps over 5 km domain of the difference between the FE and nFE scenarios ($RB_{FE} - RB_{nFE}$), averaged over 24 h, from dawn to dawn, from 10:00 UTC for **(a)** 14 September, **(b)** 18 and **(c)** 23 September 2012. **(d–f)** time-series of change in radiative balance from Ctrl scenario (ΔRB) averaged over the 5 km domain at each hour of simulation. Calculations of derived variables are explained in AppendixA.

ACPD
15, 27449–27499, 2015

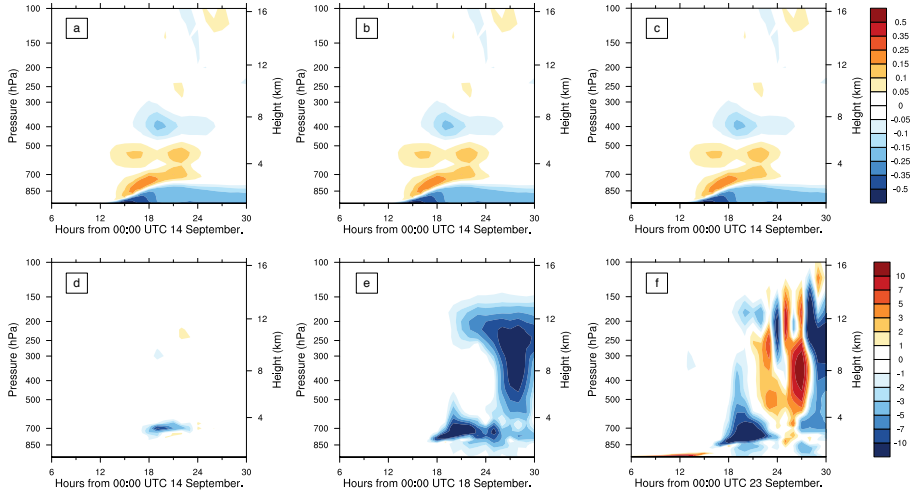

Figure 6. Difference plots between the FE and nFE scenarios with data averaged over interpolated pressure levels with 20hPa spacing, excluding the 10 grid cells at each domain border to remove the influence of boundary conditions. **(a–c)** difference in potential temperature θ (K), **(d–e)** difference in sum of all cloud variables (QCLOUD + QRAIN + QICE + QGRAUP + QSNOW; mg kg^{-1}). **(a)** and **(d)** from 06:00 UTC 14 September; **(b)** and **(e)** from 06:00 UTC 18 September; **(c)** and **(f)** from 06:00 UTC 23 September 2012.

ACPD
15, 27449–27499, 2015

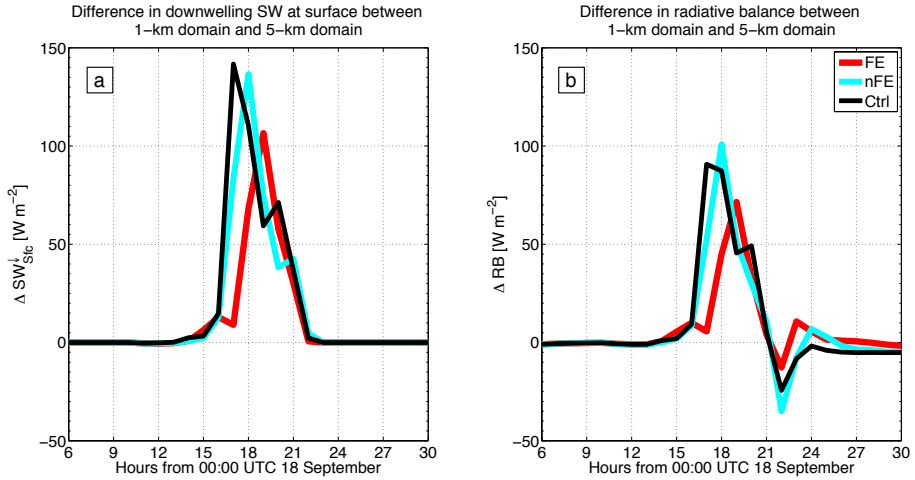

Figure 7. Comparing changes to downwelling SW radiation and radiative balance due to horizontal resolution for 18 September 2012. **(a)** Difference in downwelling SW radiation at surface between the 1 km domain and same region covered by the 5 km domain ($\Delta SW^{\downarrow}_{Sfc}$). **(b)** Difference in net radiative balance between 1 km domain and same region covered by 5 km domain (ΔRB).

ACPD
15, 27449–27499, 2015

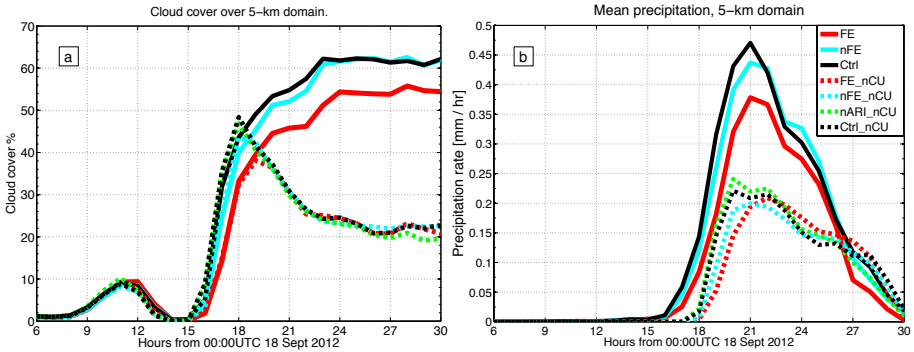

Figure 8. Cloud cover and precipitation over 5 km domain on 18 September 2012, comparing impact of biomass burning aerosol with the use of convective parameterisation. **(a)** shows percentage of domain covered by cloud, **(c)** mean precipitation rate over 5 km domain. Solid lines show simulations with convective parameterisation on, dashed line with the convective parameterisation off.

ACPD
15, 27449–27499, 2015

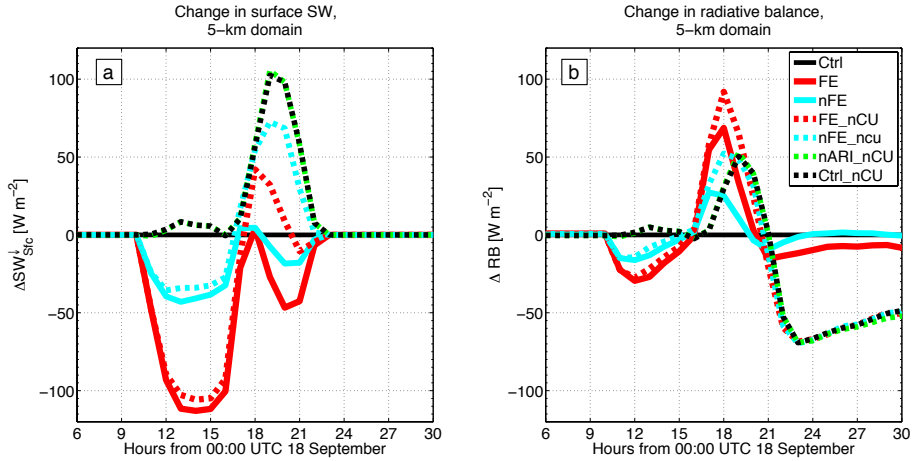

Figure 9. Comparing changes to radiative balance due to aerosol fields and cumulus physics parameterisation over the 5 km domain for 18 September 2012. **(a)** Difference in downwelling SW radiation at surface to the Ctrl scenario ($\Delta SW^{\downarrow}_{Sfc}$). **(b)** Change in net radiative balance from the Ctrl scenario (ΔRB). Solid lines for runs with cumulus physics parameterisation turned on, dashed lines with cumulus physics parameterisation turned off.

ACPD
15, 27449–27499, 2015

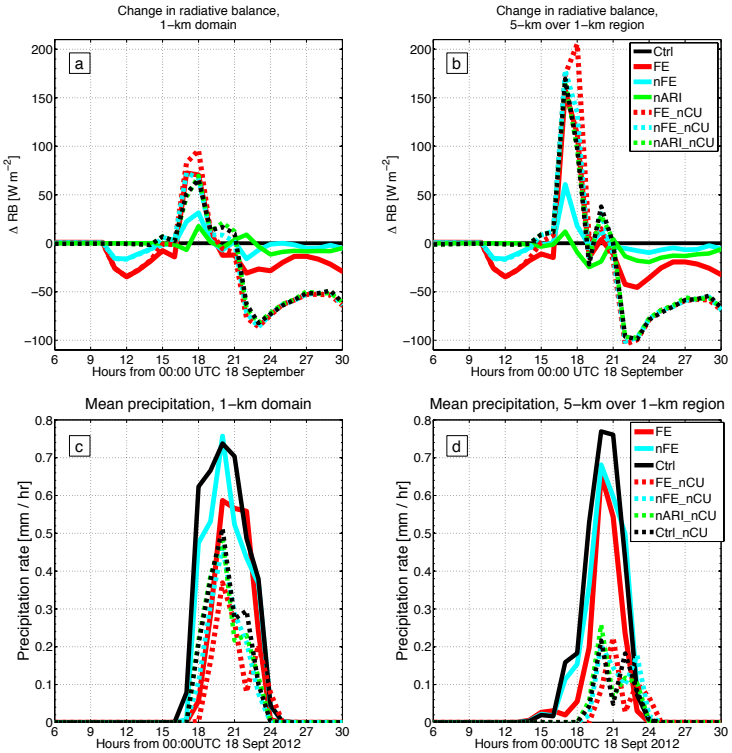

Figure 10. Net radiative balance (ΔRB) and mean precipitation rate on 18 September 2012, over the 1 km domain region, comparing aerosol effects to use of convective parameterisation on the 5 km domain. **(a)** average ΔRB over the 1 km domain, **(b)** average ΔRB from the 5 km domain over the region covered by the 1 km domain. **(c)** mean precipitation rate over the 1 km domain, **(d)** mean precipitation rate from the 5 km domain over the region covered by the 1 km domain. Solid and dot–dashed lines for runs with convective parameterisation turned on on the 5 km domain, dashed lines with convective parameterisation turned off.

ACPD
15, 27449–27499, 2015

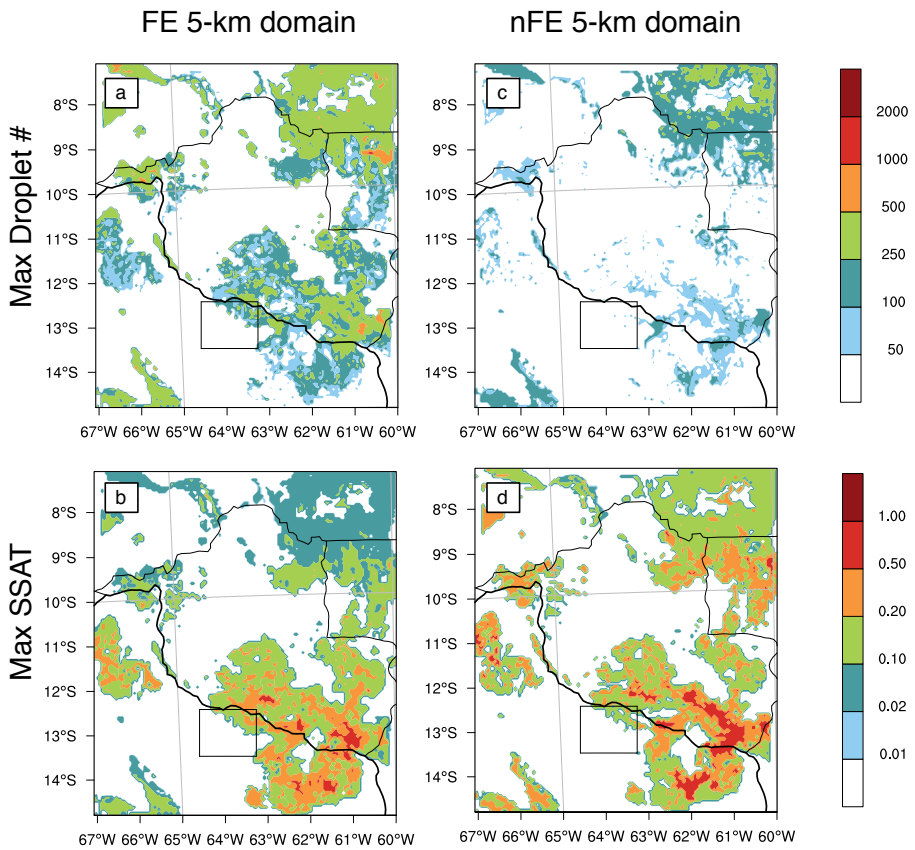

Figure 11. Comparison of maximum droplet number in column $N_{d,\,max}$ (cm^{-3}) and estimated maximum cloud supersaturation S_{max} (%) between the FE and nFE scenarios over the 5 km domain on 10:00 UTC (approximately 06:00 LT) 23 September 2012. A and C plots of $N_{d,\,max}$; B and D plots of S_{max}. A and B for FE scenario, C and D for nFE scenario.

ACPD
15, 27449–27499, 2015

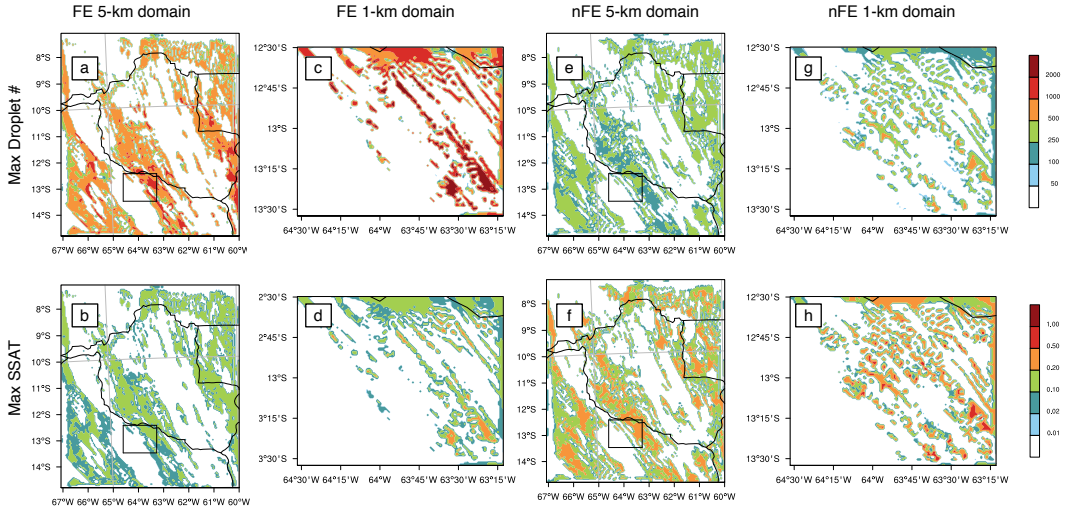

Figure 12. Comparison of maximum droplet number $N_{d,\,max}$ (cm^{-3}) and maximum cloud supersaturation S_{max} (%) between the FE and nFE scenarios over the 5 and 1 km domains on 18:00 UTC (approximately 14:00 LT) 18 September 2012. **(a)**, **(c)**, **(e)** and **(g)** plots of $N_{d,\,max}$; **(b)**, **(d)**, **(f)** and **(h)** plots of S_{max}. **(a–d)** for FE scenario, **(e–h)** for nFE scenario.

ACPD
15, 27449–27499, 2015